A comparison of viral strategies and model systems to target norepinephrine neurons in the locus coeruleus reveals high variability in transgene expression patterns

Chantal Wissing[1,2*], Lena S. Eschholz[1,3*], Maxime Maheu[1,4], Kathrin Sauter[1], Fabio Morellini[5], Simon Wiegert[1,3#], Alexander Dieter[1,3#]

[1]*Synaptic Wiring Lab, Center for Molecular Neurobiology, University Medical Center Hamburg-Eppendorf, Hamburg, Germany*
[2]*Institute for Systems Physiology, Faculty of Medicine, University Clinic, Cologne, Germany*
[3]*Department of Neurophysiology, MCTN, Medical Faculty Mannheim, Heidelberg University, Mannheim, Germany*
[4]*Section Computational Cognitive Neuroscience, Department of Neurophysiology and Pathophysiology, University Medical Center Hamburg-Eppendorf, Hamburg, Germany*
[5]*Research Group Behavioral Biology, Center for Molecular Neurobiology, University Medical Center Hamburg-Eppendorf, Hamburg, Germany*

*equal contribution, #shared correspondence:
simon.wiegert@medma.uni-heidelberg.de, alexander.dieter@medma.uni-heidelberg.de

Keywords

Locus coeruleus, Norepinephrine, Noradrenaline, viral transduction, ectopic expression, *Dbh*^{cre}, *Net*^{cre}, *Th*^{cre}, PRS×8, fiber photometry, optogenetics

Blurb: This study reports substantial heterogeneity in transgene expression patterns when using different strategies to virally transduce noradrenergic neurons of the locus coeruleus, highlighting the need to carefully validate each experimental approach in order to avoid misinterpretations when studying locus coeruleus function.

Highlights

- Heterogeneous expression patterns with different targeting strategies for LC-NE neurons
- Substantial ectopic transgene expression observed in some approaches
- No behavioral alterations in heterozygous cre mice as compared to wild-types
- PRS×8-driven reporters, indicators and actuators as a resource to investigate LC function

Abstract

The locus coeruleus (LC) norepinephrine (NE) system is involved in a variety of physiological and pathophysiological processes. Refining our understanding of LC function largely relies on selective transgene expression in LC-NE neurons, allowing targeted manipulation and readout of noradrenergic neurons. Here, we performed a side-by-side comparison of the most commonly used strategies to genetically target the LC, including different cre driver lines and promoter-mediated transgene expression. We report differences between these strategies in terms of transgene expression efficacy and specificity. Parallelly, we found no behavioral alterations in cre-expressing mice of any mouse line compared to wild-type littermates. Finally, to further facilitate the investigation of LC-NE function, we created a suite of constructs, including a reporter protein, a calcium indicator, and a light-driven cation channel, whose expression is mediated by the previously described PRS×8 promoter. These constructs allow identification, monitoring, and manipulation of LC-NE activity either in wild-type mice, or in combination with tissue-specific manipulations of different cre driver lines. The results of our study are crucial for the interpretation of previous experiments using the respective targeting strategies, as well as for the design of future studies.

Introduction

The locus coeruleus (LC) — a bilateral nucleus located in the brainstem — is the major source of norepinephrine (NE; also: noradrenaline) in the central nervous system. Despite its small size (~3,000 neurons in the rodent brain[1]), the LC is involved in several physiological functions, including alertness, arousal, sensory perception, attention, learning, and memory consolidation[2–4]. In addition, the LC has been implicated in numerous pathological conditions including depression, post-traumatic stress disorder, Alzheimer's disease, and Parkinson's disease[2–6]. Accordingly, the LC-NE system is currently the subject of detailed investigations[2,3,7–9]. Recent research suggests this nucleus is modular, with subpopulations of cells targeting different brain regions, presumably with different physiological roles[2,10,11]. Thus, the LC may exert a more sophisticated, target-specific modulation of brain activity than previously thought. These findings have brought the LC-NE system into the focus of many research groups that rely on the specific targeting of LC-NE neurons to interrogate LC function[2].

Key technologies to access the LC-NE system in animal models include genetic tools such as cre driver lines (Supplementary Table S1) and viral transduction, either with conditional constructs, or with tissue-specific promoters. These methods allow gene expression in molecularly identified neural populations, even in a projection-specific manner[12]. Detailed studies of the LC-NE system are more feasible than ever with the recent development of genetically encoded sensors for norepinephrine[13,14] and dopamine[15–17], as well as opto- or chemogenetic strategies that allow the manipulation of LC subpopulations in a projection-specific manner. Driver lines have been developed to express cre recombinase under the control of the dopamine-β-hydroxylase (DBH) promoter in mice[18,19] and rats[20],

under control of the norepinephrine transporter (NET) in mice[21], and several mouse[18,22,23] and rat[24] driver lines exist that express cre recombinase under the control of the tyrosine hydroxylase (TH) promoter. DBH catalyzes the synthesis of NE from dopamine (DA) and is therefore specific for NE neurons. Similarly, NET, the membrane protein that mediates reuptake of extracellular NE, is used as a selective marker for NE-releasing neurons. In contrast, TH is the enzyme involved in the synthesis of L-DOPA from tyrosine, three reaction steps upstream of the end product NE, and is therefore present in all catecholaminergic cells, including dopaminergic ones.

Alternative approaches to target the LC-NE system that do not rely on transgenic lines have also been proposed. In particular, NE-specific transgene expression has been achieved using a minimal synthetic promoter, containing 8 copies of a cis-regulatory element (Phox2a/Phox2b response site; PRS) derived from the human *Dbh* promoter, thus termed PRS×8[25]. This promoter has been shown to be specific for noradrenergic cells in both mice[26,27] and rats[25,28]. While the four strategies (*Dbh*^{cre}, *Net*^{cre}, *Th*^{cre}, and PRS×8) for targeting the LC-NE system provide a wide range of alternatives to choose from, they come with different caveats and challenges (see e.g., [29–31] for reviews on transgene expression strategies). Critically, a direct comparison of the most commonly used LC-NE targeting strategies is lacking, and proper quantification of viral transduction is not always reported.

Here, we performed a side-by-side comparison of virus-mediated transgene expression in the LC-NE system by introducing cre-dependent reporter genes into the LC of *Dbh*^{cre}, *Net*^{cre}, and *Th*^{cre} mice, and unconditional reporter genes under the control of the PRS×8-promoter into the LC of wild-type mice. We report substantial differences in transgene expression, both in terms of efficacy and molecular specificity, while we did not detect any behavioral changes associated with cre expression in any of the mouse lines tested. To facilitate investigations of the LC-NE system, we have developed a suite of PRS×8-driven tools including a fluorophore (eGFP), a calcium indicator (jGCaMP8m), and a red-light sensitive channelrhodopsin (ChrimsonR) that allow tissue-specific transgene expression. These tools can be used either in wild-type mice or in combination with cre driver lines, thereby facilitating simultaneous transgene expression in additional neuronal populations[32]. Our findings have broad implications for researchers using genetic manipulation of the noradrenergic system to study LC function: they may guide the choice of an appropriate targeting strategy in future research, and may assist in the interpretation of data obtained from the respective model system.

Results

Efficacy and specificity of transgene expression across model systems

To visualize transgene expression in the LC-NE system, we bilaterally injected the LC with titer-matched suspensions of recombinant adeno-associated virus (rAAV2/9) encoding enhanced green fluorescent protein (eGFP; Fig. 1a). In *Dbh*^{cre}, *Net*^{cre} and *Th*^{cre} mice, cre-dependent gene expression was controlled by combining double-floxed inverted open reading frames (DIO)[33]

113 of the transgene with a strong, synthetic promotor (CAG)[34]. In wild-type mice (C57BL/6J), the
114 reporter gene was expressed under the control of the synthetic PRS×8 promoter. Six weeks
115 after injection, we analyzed eGFP expression by fluorescence microscopy of coronal sections
116 which were immuno-stained against TH (to visualize NE-expressing neurons) and GFP (to
117 enhance the signal originating from transgene expression; Fig. 1b). To quantify transgene
118 expression at a cellular level, cells expressing TH (TH^+) or eGFP ($eGFP^+$) were automatically
119 segmented using the deep learning-based algorithm *CellPose*[35,36] (Fig. 1c).

120 To assess the ability to selectively target the LC, we evaluated the *efficacy* and
121 *specificity* of viral transduction of LC-NE neurons. To this end, we compared the overlap
122 between masks segmented in the TH and GFP channel, respectively, defining cells with an
123 overlap of ≥ 50% as co-expressing. Efficacy is defined as the proportion of TH^+ cells co-
124 expressing eGFP, while specificity reports the proportion of $eGFP^+$ cells co-expressing TH.

125 We found differences in the efficacy between model systems (one-way ANOVA,
126 $F_{24} = 14.71$, $p = 1.2 \times 10^{-5}$; Fig. 1d): while no significant differences in efficacy were detected
127 between *Dbh*^{cre}, *Net*^{cre} and PRS×8-mediated transgene expression (70.5 ± 11.8 %, 79.5 ± 9.0
128 %, 78.2 ± 12.9 %; mean ± SD; Tukey's test, p = 0.68/0.77/0.99 for *Dbh*^{cre} vs *Net*^{cre}/*Dbh*^{cre} vs
129 PRS×8/*Net*^{cre} vs PRS×8), the efficacy of *Th*^{cre} mediated expression was significantly lower than
130 the other model systems (33.3 ± 22.7%; Tukey's test, $p = 6 \times 10^{-4}/3 \times 10^{-5}/5 \times 10^{-5}$, compared
131 against *Dbh*^{cre}/*Net*^{cre}/PRS×8, respectively). We further noted a large variability in the efficacy
132 of GFP expression in *Th*^{cre} mice, with one mouse even showing an efficacy of up to 75%, while
133 the efficacies of other mice — even from the same litter — was below 20 % (Fig. S1).

134 We also found differences in specificity (one-way ANOVA, $F_{24} = 14.47$, $p = 1.4 \times 10^{-5}$)
135 between model systems (Fig. 1e): Here, the specificity of *Th*^{cre} mediated expression
136 (46.0 ± 12.1 %) was significantly lower than *Dbh*^{cre} (82.2 ± 9.5 %), *Net*^{cre} (71.4 ± 13.6 %), and
137 PRS×8 (65.2 ± 5.0 %) mediated transgene expression (Tukey's test, $p = 7 \times 10^{-6}/ 7 \times 10^{-4}/0.01$
138 *Dbh*^{cre}/*Net*^{cre}/PRS×8 against *Th*^{cre}). Furthermore, the *Dbh*^{cre} approach was significantly more
139 specific than PRS×8 mediated transgene expression (Tukey's test, p = 0.03). No significant
140 differences were found between *Dbh*^{cre} vs. *Net*^{cre} and between PRS×8 vs. *Net*^{cre}.

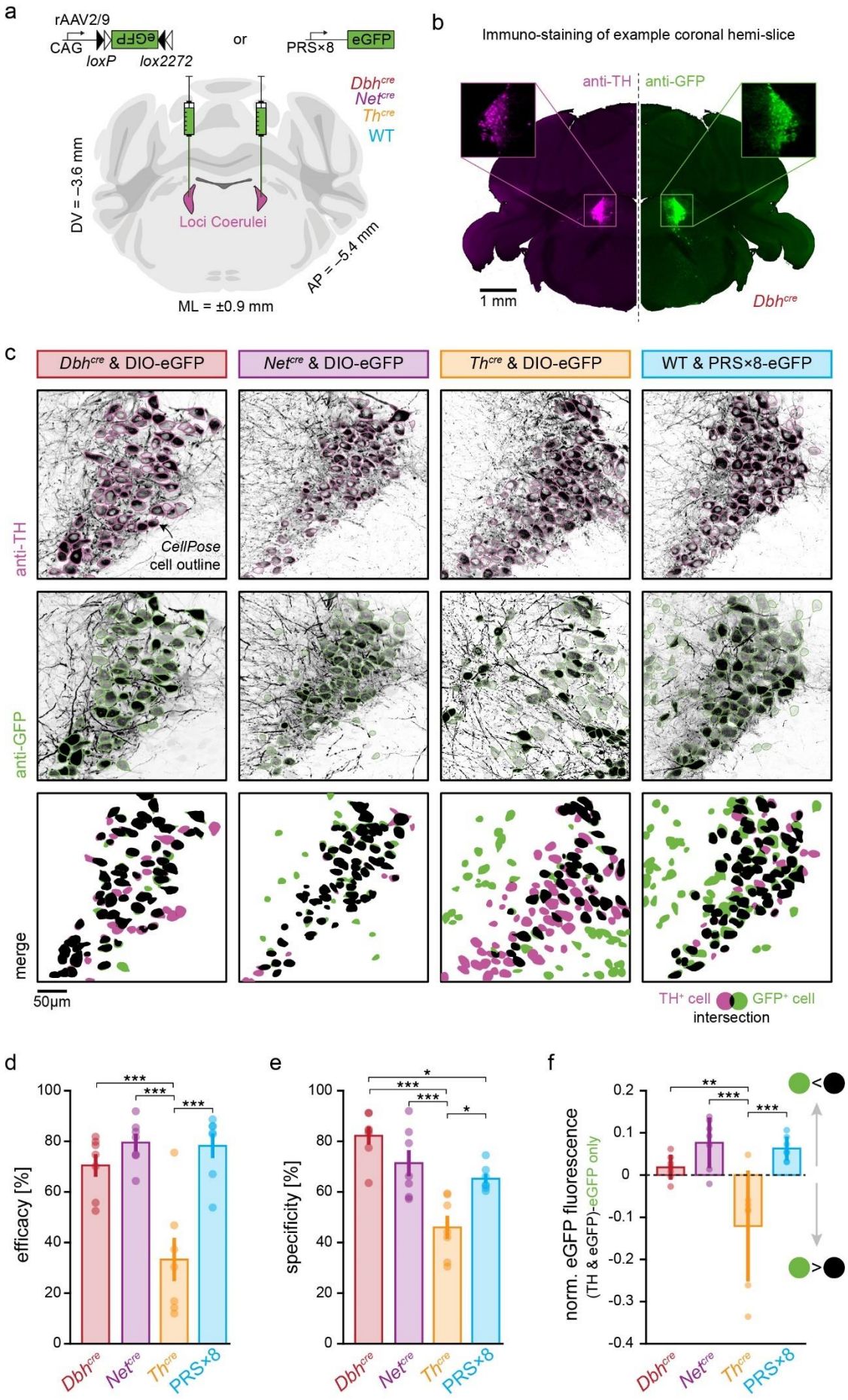
a
rAAV2/9
CAG
eGFP
loxP
lox2272
or
PRS×8
eGFP
Dbh^cre
Net^cre
Th^cre
WT
DV = −3.6 mm
Loci Coerulei
AP = −5.4 mm
ML = ±0.9 mm
b
Immuno-staining of example coronal hemi-slice
anti-TH
anti-GFP
1 mm
Dbh^cre
c
Dbh^cre & DIO-eGFP
Net^cre & DIO-eGFP
Th^cre & DIO-eGFP
WT & PRS×8-eGFP
anti-TH
anti-GFP
merge
CellPose
cell outline
50µm
TH+ cell
GFP+ cell
intersection
d
efficacy [%]
Dbh^cre
Net^cre
Th^cre
PRS×8
e
specificity [%]
f
norm. eGFP fluorescence
(TH & eGFP)-eGFP only

141

Figure 1 | Viral transduction of LC-NE neurons in different model systems. a, Either CAG-DIO-eGFP (in *Dbh*^{cre}, *Net*^{cre}, and *Th*^{cre}) or PRS×8-eGFP (in WT) was bilaterally injected into the LC of mice (n = 7 animals in each group). Coronal brain slice image from [37] **b**, Example LC hemi-brain slice (vertically mirrored) from a *Dbh*^{cre} animal. Noradrenergic neurons were identified by immunostaining against TH (left, magenta), while transgene expression was visualized with an anti-GFP staining (right, green). **c**, Example LC cells in each of the four model systems (columns) immuno-stained against TH (first row, magenta outlines) and GFP (second row, green outlines). Cells were identified with *CellPose* and boundaries are denoted with colored outlines. Resulting cell masks were then overlaid (third row), and each TH$^+$ cell was labeled as GFP$^+$ (successful transduction, black) when cell masks overlapped 50% or more the size of the TH$^+$ cell, or GFP$^-$ otherwise (missed transduction, magenta). GFP$^+$ and TH$^-$ (erroneous transduction, green) was counted as unspecific transduction. **d**, Efficacy (i.e., the true positive rate), computed as N(GFP$^+$|TH$^+$) / N(TH$^+$), across model systems. **e,** Specificity (i.e., the inverse of the false positive rate), computed as N(TH$^+$|GFP$^+$) / N(GFP$^+$), across model systems. **f,** Difference in normalized eGFP fluorescence of neurons that co-expressed eGFP and TH (i.e., true positive neurons) and neurons that expressed eGFP only (i.e., false positive neurons) across model systems. Negative values indicate that eGFP fluorescence of TH negative neurons was brighter than eGFP fluorescence of TH expressing neurons. In **d-f** error bars denote the standard error of the mean (with n = 7), while statistical significance is denoted by */**/*** for $p < 0.05/0.01/0.001$, respectively. Only significant differences are indicated. Numerical data underlying panels d-f can be found in supplementary material 1 (S1_Data.xlsx).

In addition to differences in the efficacy of transgene expression and its specificity to TH$^+$ neurons, we realized that also the levels of transgene expression in relation to the levels of endogenous TH expression differed across approaches. While the averaged normalized eGFP fluorescence in true positive neurons (i.e., neurons that co-expressed eGFP and TH) was expectedly higher than in false positive neurons (i.e., neurons that expressed eGFP but not TH) in *Dbh*^{cre}, *Net*^{cre} and PRSx8 mice (0.02 ± 0.03 % / 0.08 ± 0.06 / 0.06 ± 0.03, respectively), it was lower than the eGFP fluorescence of true positive cells in *Th*^{cre} mice (- 0.12 ± 0.13), indicating that the levels of cre-mediated transgene expression are functionally de-coupled from the levels of native TH expression in this mouse line (one-way ANOVA, $F_{24} = 10.1$, $p = 0.0002$; Fig. 1f). Similarly, at the cellular level, normalized eGFP fluorescence in true positive neurons was higher than in false positive neurons in *Dbh*^{cre}, *Net*^{cre} and PRS×8 mice, while eGFP fluorescence in false positive neurons exceeded the fluorescence of true positive neurons in *Th*^{cre} mice ($p < 0.1 \times 10^{-5}$ for all groups, Bonferroni-corrected Wilcoxon rank sum test; Fig. S2). These findings indicate that cre recombinase activity and endogenous TH expression are de-coupled in *Th*^{cre} mice, and further corroborate the heterogeneous expression patterns across approaches.

Control experiments

We performed a number of controls to validate our results and to rule out potential sources of confounding.

Effects of overlap threshold: In our analyses, we have chosen an overlap threshold between eGFP$^+$ and TH$^+$ cells of ≥50% to define co-expression. To assess the generality of our results, we systematically varied the threshold from 5 to 95% (in 5% increments). Relative differences in both efficacy and specificity were independent of the overlap threshold in this range (Fig. S3).

Effects of leaky virus expression: One factor that may lead to underestimation of transduction specificity in cre lines is non-specific transgene expression of cre-dependent

constructs in cre-negative cells, as previously described[38]. To assess the extent of this effect, we bilaterally injected the same rAAV2/9-CAG-DIO-eGFP in the LC of 2 wild-type mice. We could not detect eGFP-expressing cells in these animals, ruling out leaky expression of our viral constructs at the titers used in this study (Fig. S4).

Effects of cell segmentation errors: To account for potential segmentation errors, we compared results obtained from *CellPose* with manual cell identification by two independent experimenters (CW and AD) in a subset of slices and found agreement between *CellPose* and experimenter rating, as well as between experimenters (Fig. S5). Of note, the training data for *CellPose* was annotated by a third experimenter (LSE), which eliminated experimenter effects. To further validate our experimental routine and our analysis pipeline, we injected rAAV2/9-CAG-DIO-eGFP also into the ventral tegmental area (VTA) of Th^{cre} mice (Fig. S6a-b). In the VTA, we found a specificity of 60.7 ± 6.8 % (Fig. S6c-d), which is in line with the specificity reported by Lammel and colleagues[39] (59 ± 1 %; based on visual inspection), and further confirms that our automated analysis is comparable to manual curation by a human observer.

Effects of GFP staining: To investigate the role of GFP staining in our findings, we used a secondary antibody in the red spectrum against our primary anti-GFP staining and directly compared cells detected in the green (native eGFP) and red (GFP-stained) channels in a subset of animals (Fig. S7a). We found that the anti-GFP staining increased the number of cells detected by *CellPose* by 21.5 ± 15.3% (*t*-test against 0: $t_{14} = 4.8$, $p = 2.8 \times 10^{-4}$; Fig. S7b), and that the averaged normalized brightness of stained cells exceeded the one of native eGFP-expressing cells by 55.0 ± 35% (*t*-test against 0: $t_{14} = 6.66$, $p = 1.08 \times 10^{-5}$; Fig. S7c). This change in fluorescence was significantly stronger in the dimmest eGFP-expressing cells, i.e., cells expressing relatively low levels of eGFP (*t*-test against 1: $t_{12} = -11.56$, $p = 1.5 \times 10^{-8;}$ Fig. S7d-e). Unfortunately, it is unclear whether low levels of native eGFP expression are due to low promoter activity or weak viral transduction. If low promoter activity causes low eGFP levels, the transgene should accumulate over time, as even low levels of cre recombinase will eventually recombine all floxed genes. Hence, the GFP staining would compensate for the number of detected cells. In contrast, if low eGFP levels result from differences in viral transduction of individual cells, i.e., directly reflects the number of transgene copies per cell, the GFP staining would inflate the number of detected cells. Of note, the changes in fluorescence and cell detection introduced by the anti-GFP staining apply to all experimental groups in the same way.

Ectopic expression of transgenes

In addition to differences in the specificity of neural transduction within the LC and its immediate surroundings, we also observed ectopic GFP expression in various brain regions more distant from the LC (Fig. 2). Again, we found differences between the different model systems with respect to peri-LC transgene expression. The lowest ectopic expression was found in Dbh^{cre} animals, where we observed *GFP* expression only in small numbers of cells in

the cerebellum (< 10 neurons, 3/7 animals; Fig. S8a) and in the inferior colliculus (< 10 neurons, 1/7 animals; Fig. 2a). In *Net*^{cre} mice, we found a small number of GFP expressing cells in the cerebellum (< 10 neurons, 4/7 mice Fig. 2b), and moderate GFP expression in the vestibular nucleus of a single mouse (~10-100 neurons, Fig. S8b). In *Th*^{cre} mice, we found substantial ectopic expression in the lateral parabrachial nucleus (~10-500 neurons, 7/7 mice; Fig. S8c), moderate expression in the inferior colliculus (10-100 neurons, 2/7 mice; Fig. 2c) and central gray (< 100 neurons, 1/7 mice; Fig. S8d) and low expression in the cerebellum (< 10 neurons, 1/7 mice; Fig. S8e). Finally, in PRS×8 animals, we found moderate GFP expression both in the vestibular nucleus (~10-200 neurons, 6/7 animals; Fig. S8f), and in the lateral parabrachial nucleus (~10-100 neurons, 3/7 animals; Fig. 2d).

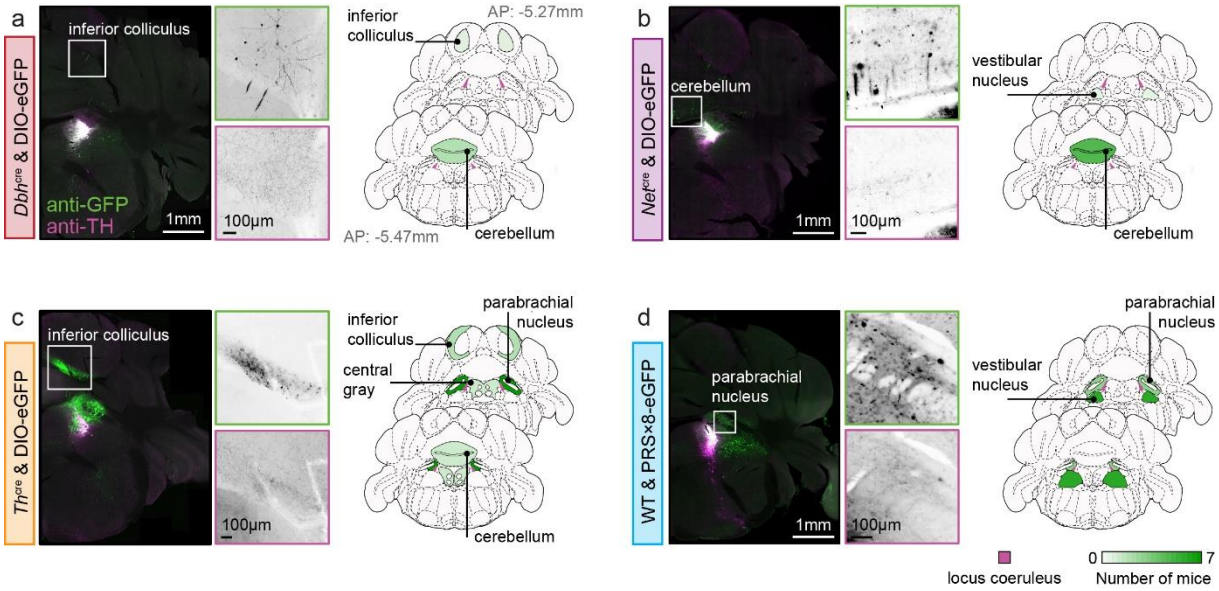

Figure 2 | Ectopic transgene expression across model systems. a-d, On the left panels: example brain slices showing ectopic expression in *Dbh*^{cre}/*Net*^{cre}/*Th*^{cre}/PRS×8 model systems. Immuno-straining against GFP and TH is displayed in green and magenta, respectively. On the right panels: summary of ectopic expression across all mice in *Dbh*^{cre}/*Net*^{cre}/*Th*^{cre}/PRS×8 model systems. Brain regions are color-coded to reflect the number of mice which showed ectopic expression (at least 1 neuron) in the corresponding brain region. Brain slice images from [37].

Effects of promoter, serotype, and injection volume on transduction of LC-NE neurons

Next, we systematically varied the promoter controlling transgene expression, the serotype of the rAAV, and the volume of injected virus suspension, in order to investigate potential effects of these parameters on the transduction of LC-NE neurons.

Effects of promoter: We first assessed whether the choice of the promoter had an influence on the efficacy and specificity of transgene expression in LC-NE neurons. The human synapsin (hSyn) promoter[40,41] is a relatively small promoter, which has been widely used in neuroscientific research, and it facilitates transgene expression broadly across all neuronal

252 subtypes. Thus, we injected an additional set of *Dbh*^{cre} mice (n = 7) with rAAV2/9 encoding
253 eGFP in a cre-dependent manner under control of the hSyn promoter (rAAV2/9-hSyn-DIO-
254 eGFP; Fig. 3a). We observed robust eGFP expression in all injected LC (Fig. 3b), and could not
255 detect significant differences between *Dbh*^{cre} mice injected with rAAV2/9-hSyn-DIO-eGFP and
256 rAAV2/9-CAG-DIO-eGFP, neither in terms of efficacy (78.5 ± 4.3 vs. 70.5 ± 11.8, p = 0.12, two-
257 sample t-test; Fig. 3c) nor in terms of specificity (83.5 ± 10.5 vs. 82.2 ± 9.5, p = 0.82, two-
258 sample t-test; Fig. 3d). Hence, our findings are not restricted to the CAG promoter, and reliable
259 transgene expression in LC-NE cells of *Dbh*^{cre} mice can also be achieved under control of hSyn.

260 *Effects of viral serotype:* Since transgene expression in *Th*^{cre} mice, and to a lower degree
261 also under the PRS×8 promoter, resulted in ectopic eGFP expression in regions distant to the
262 LC, we suggest that less viral spread can help to reduce ectopic transgene expression. It was
263 previously shown in cortical tissue that rAAV2/2 shows less spread compared to the serotypes
264 rAAV2/1, rAAV2/5, rAAV2/8, and rAAV2/9[42]. To get a precise understanding of serotype
265 effects on viral spread, we injected wild-type mice either with rAAV2/9 or rAAV2/2 encoding
266 eGFP unconditionally under control of the hSyn promoter (Fig. 3e-f, Fig. S9). The viral spread
267 of transgene expression was then quantified by smoothing, normalizing, and thresholding of
268 immune-stained hemi-brain slices. Indeed, we found that transgene expression upon viral
269 transduction using rAAV2/2 led to a more restricted spread as compared to rAAV2/9, at least
270 when thresholding fluorescence up to 0.5 of its maximum value (i.e., when analyzing regions
271 with relatively distant to the injection site; p = 0.0002/0.0002/0.0003/0.0033/0.028 for
272 thresholds of 0.1/0.2/0.3/0.4/0.5, respectively; two-sample t-test, n = 6 LC/serotype; Fig. 3g).

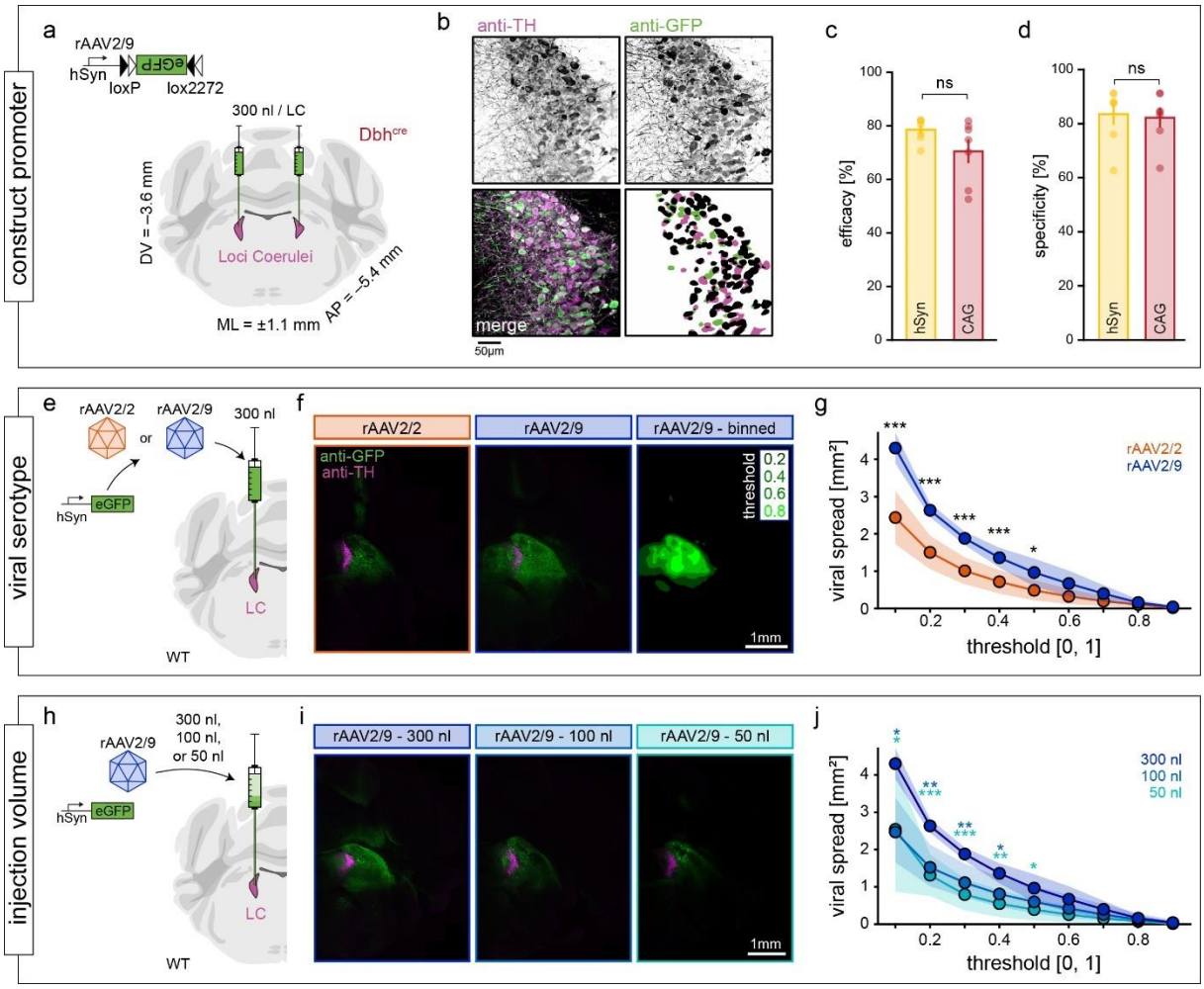

Figure 3 | Effects of promoter, serotype, and injection volume on viral transduction of LC-NE neurons. a, To investigate effects of the promoter on viral transduction, rAAV2/9-hSyn-DIO-eGFP (a construct analog to rAAV2/9-CAG-DIO-eGFP used in Fig. 1 and 2) was bilaterally injected into the LC of *Dbh*^{cre} mice (n = 7 animals). Coronal brain slice image from [37]. **b**, Example LC section from an rAAV2/9-hSyn-DIO-eGFP injected *Dbh*^{cre} mouse immuno-stained against TH (top left) and eGFP (top right), as well as color-coded overlay (bottom left). Cells were identified with *CellPose* and resulting cell masks were overlaid (bottom right), and each TH$^+$ cell was labeled as GFP$^+$ (black) when cell masks overlapped by at least 50 % , or GFP$^-$ otherwise (magenta). GFP$^+$ and TH$^-$ (green) was counted as unspecific transduction. **c**, Efficacy (N(GFP$^+$|TH$^+$) / N(TH$^+$)) and **d,** Specificity (N(TH$^+$|GFP$^+$) / N(GFP$^+$)) were comparable upon injection of hSyn-DIO-eGFP (yellow) or CAG-DIO-eGFP (red; re-plotted from Fig. 1d, 2) in *Dbh*^{cre} mice (ns = not significant; two-sample t-test, n = 7 each). **e**, To investigate effects of the viral serotype on viral transduction, 300 nl of either rAAV2/2-hSyn-eGFP or rAAV2/9-hSyn-eGFP were bilaterally injected into the LC of wild-type mice (n = 6 LC from N = 3 mice each). **f**, Example images of hemi-brain slices of an rAAV2/2-injected (orange, left) and an rAAV2/9 injected mouse (blue, center). Images were smoothed and fluorescence was normalized [x, y], before thresholding images with an increment of 0.1 and calculating the area above threshold (see example with an increment of 0.2 on the right). **g**, Viral spread was quantified at various thresholds, revealing a more restricted spread upon injection of rAAV2/2 as compared to rAAV2/9 (*/**/*** for p < 0.05/0.01/0.001, two-sample t-tests, N = 6 LC per group). **h**, To investigate effects of the injection volume on viral transduction, either 300, 100, or 50 nl of rAAV2/9-hSyn-eGFP were bilaterally injected into the LC of wild-type mice (n = 6 LC from n = 3 mice each). **i**, Example images of hemi-brain slices of mice injected with 300 nl (dark blue, left), 100 nl (light blue, center) or 50 nl of rAAV2/9-hSyn-eGFP (cyan, right). **j**, Viral spread was quantified at various thresholds, revealing a more restricted spread upon injection 100nl and 50nl of viral suspension as compared to 300 nl of viral suspension (*/**/*** for p < 0.05/0.01/0.001, one-way ANOVA and Tukey's test, N = 6 LC per group). Stars denote significance between the 300 nl group and the 100 nl/50 nl group, respectively, as no significant differences were found between the 100 nl and the 50 nl group. Numerical data underlying panels c, d, g, and j can be found in supplementary material 1 (S1_Data.xlsx).

297 *Effects of injection volume:* As an alternative to using a different viral serotype, we
298 aimed to reduce viral spread by lowering the injection volume. In these experiments, we
299 bilaterally injected either 300 nl (the standard volume used in other experiments in this
300 manuscript), 100 nl, or 50 nl of rAAV2/9-hSyn-eGFP into the LC of wild-type mice (Fig. 3h-I,
301 Fig. S9) and quantified the viral spread as described above. Significant differences in viral
302 spread were observed for thresholds up to 50% of the maximum fluorescence (one-way
303 ANOVA, F_{15} = 5.3/13.9/13.6/8.63/4.38, p = 0.02/0.0004/0.0004/0.003/0.03 for thresholds of
304 0.1/0.2/0.3/0.4/0.5, respectively; Fig. 3j). More specifically, the viral spread upon injection of
305 100 nl of viral suspension was significantly lower as compared to the spread of 300 nl for
306 thresholds up to 0.4 (p = 0.03/0.002/0.007/0.04, Tukey's test), while the spread upon injection
307 of 50 nl was significantly lower as compared to 300 nl for thresholds up to 0.5 (p =
308 0.04/0.0005/0.0004/0.003/0.03, Tukey's test). No significant differences between the viral
309 spread following from 50 nl and 100 nl injections were found at any threshold.

310 These experiments demonstrate that the viral spread observed upon LC injections can
311 be reduced both by implementing serotype rAAV2/2 and by lowering the injection volume of
312 viral suspension. Hence, the use of serotype rAAV2/2 or lower injection volumes might help
313 to reduce ectopic expression in model systems that showed ectopic expression in brain
314 regions distant to the LC (i.e., *Th*^{cre} and, to a milder degree, PRS×8)

315

316 *Success rates of LC targeting*

317 Occasionally, we observed complete absence of the GFP signal (i.e., transgene expression) in
318 one of the two LC of bilaterally injected animals, while expression was strong in the second
319 LC. This pattern of unilateral transgene expression was found in 3/2/1/3 out of each 5
320 *Dbh*^{cre}/*Net*^{cre}/*Th*^{cre}/PRS×8 mice, respectively (Fig. 4a). Since we used the same micropipette to
321 inject the viral suspension sequentially in both LC, we were concerned that this approach
322 might have compromised the success rate of injections (e.g., due to possible inhomogeneous
323 distribution of viral particles in the suspension). Therefore, we added two more mice to each
324 group using a new micropipette for each LC. However, also here, we observed unilateral
325 transgene expression in some cases (0/0/2/1 *Dbh*^{cre}/*Net*^{cre}/*Th*^{cre}/PRS×8; Fig. 4b), which did not
326 statistically differ from the previous group where the same pipette was used (p = 0.72, chi-
327 squared test, n = 20/8 mice; Fig. 4c). Thus, sequential injection with the same pipette did not
328 explain occasional failure of virus transduction. Importantly, infusion of the viral suspension
329 was also visually confirmed during each injection, and hence the absence of expression in
330 some LC could not be attributed to clogged micropipettes.

331 The overall success rate of injections in our study (80%, 59/74 LC) is in line with
332 previous reports (76-80%)[43,44], which attributed the lack of transgene expression to off-target
333 virus administration (i.e., injection in brain regions adjacent to LC). To test this possibility, we
334 injected *Dbh*^{cre}, *Net*^{cre}, and *Th*^{cre} mice (n = 3 each) with a so-called 'cre-switch' construct which
335 consists of a double-floxed open reading frame for tdTomato and an inverted open reading

336 frame for eGFP (DO-tdTomato-DIO-eGFP)[45]. Hence, cell type specific expression of eGFP in cre
337 positive cells allows for characterization of the molecular specificity, while expression of
338 tdTomato in cre negative cells allows for estimation of the general viral spread (and potential
339 off-target virus administration) at the injection site (Fig. 4d). Four weeks after injection,
340 expression of tdTomato in cre negative cells revealed a broad viral spread in most animals,
341 reaching from the midline to the parabrachial nucleus in the mediolateral axis, and from the
342 4th ventricle to the central gray in the dorsoventral axis (Fig. 4e). However, also in these
343 experiments we observed 3 animals (out of 9) with unilateral eGFP expression where also
344 tdTomato was absent in the non-expressing hemisphere (Fig. 4f), suggesting that absence of
345 expression in LC was not due to off-target injection in neighboring brain tissue but rather a
346 failure of virus infection in general.

347 We therefore suggest that the lack of expression in some LC might result from off-
348 target administration into the 4th ventricle, which is in close proximity to the LC. This
349 mistargeting could result from minor misalignment on the mediolateral axis during virus
350 injection, resulting in more lateral virus injection in one hemisphere, but virus injection into
351 the 4th ventricle in the other hemisphere. Indeed, when changing the injection coordinates
352 from ± 0.9 mm to ±1.1 mm lateral relative to bregma in subsequent experiments (i.e., injection
353 of AAV2/9-hSyn-DIO-eGFP in *Dbh^{cre}* mice and injection of AAV2/2 or AAV2/9-hSyn-eGFP in WT
354 mice; see Figs. 3 and S9), we observed bilateral transgene expression in 7/7 and 12/12 LC (Fig.
355 4f-g). These success rates are significantly higher than the ones observed when injecting ±0.9
356 mm lateral relative to bregma (Fig. 4h-i). Thus, more laterally targeted injections lead to
357 increased transduction rates of the LC, likely by lowering the risk of injecting the virus
358 suspension into the 4th ventricle.

359

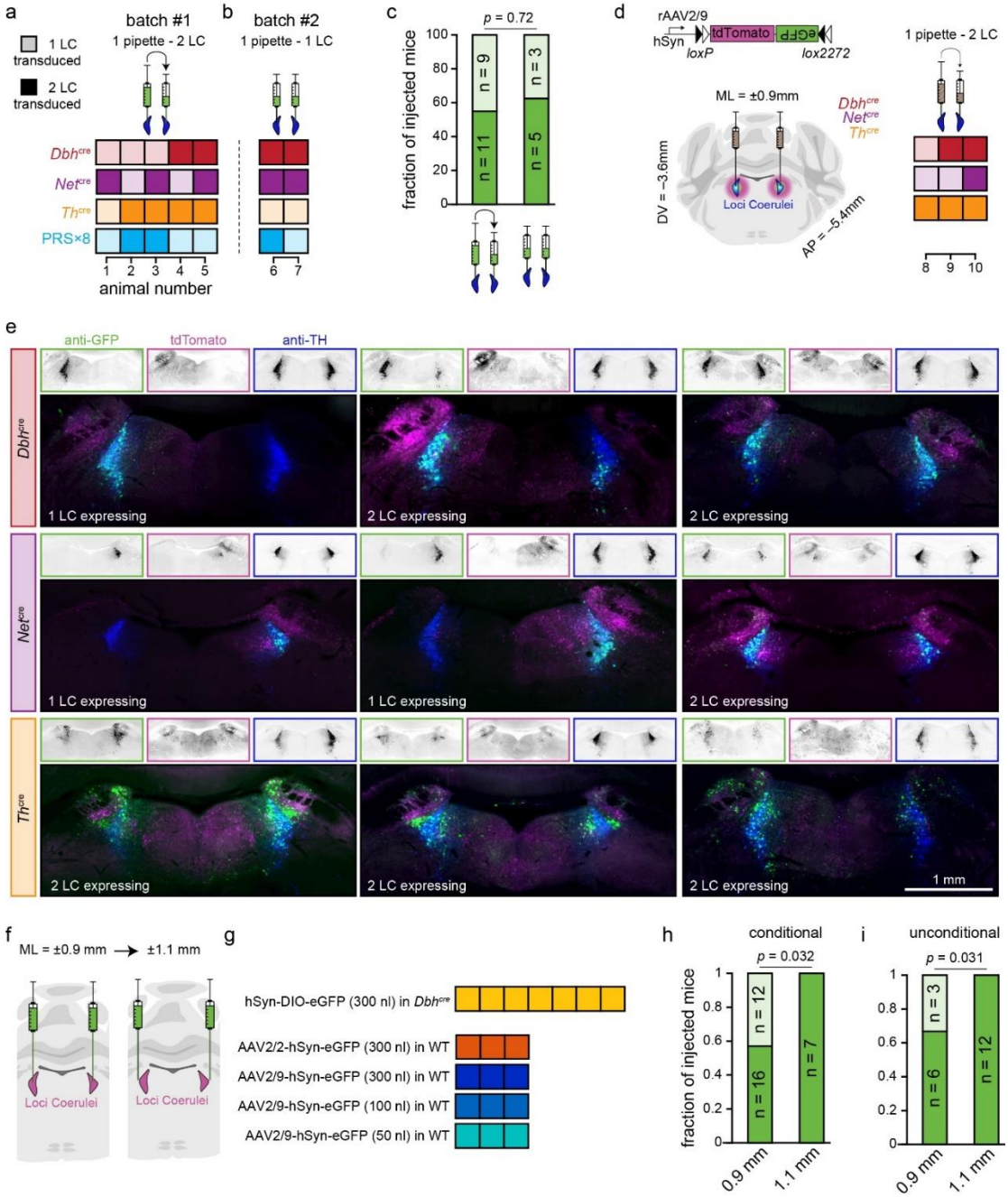

Figure 4 | Improving LC targeting. a, Bilateral transduction efficacy (n = 5 animals in each group) using a single micropipette to sequentially infect both LC (2 × 300nL). **b**, Same as a, except that one micropipette was used for each LC (n = 2 animals in each group). **c**, Fraction of animals with bilateral (solid) or unilateral (shaded) LC transduction upon LC injections with a single pipette vs 2 pipettes. **d**, Estimation of viral spread by injections of a 'cre-switch' construct leading to eGFP expression in a cre-dependent manner and tdTomato expression in cre-negative cells[45]. **e**, Transgene expression in *Dbh*^{cre}, *Net*^{cre} and *Th*^{cre} animals (n = 3 animals each) shows conditional eGFP expression in cre positive cells (green) and tdTomato expression in cre-negative cells (magenta). LC-NE cells are visualized by immunostaining against TH (dark blue). Importantly, in animals without eGFP expression, cre-negative cells around the LC also lacked the expression of tdTomato, suggesting likely resulting from loss of the virus suspension to the ventricle. **f,** Change of mediolateral coordinates for virus injections from ±0.9 mm to ± 1.1 mm. **g**, Bilateral transduction efficacy after using the new coordinates in transgenic or wild-type animals. **h**, Fraction of conditionally eGFP-expressing animals with bilateral (solid) or unilateral (shaded) LC transduction upon LC injections at mediolateral coordinates of from ±0.9 mm and ± 1.1 mm (e.g., pooled data from panel a/b vs panel g, uppermost row). **i**, Fraction of unconditionally fluorophore-expressing animals with bilateral (solid) or unilateral (shaded) LC transduction upon LC injections at mediolateral coordinates of from ± 0.9 mm and ± 1.1 mm (e.g., pooled data from panel d vs panel g, row 2-5). p-values according to chi-squared test are indicated on top of each bar plot.

Behavioral screening of cre lines

Unlike the PRS×8 approach, cre-dependent transgene expression relies on the use of mouse lines expressing cre recombinase in a molecularly defined set of cells. As phenotypic alterations have been broadly reported for neuromodulatory cre driver lines[46–48], we screened the driver lines used in this study for behavioral alterations. We applied a series of well-established behavioral paradigms to quantify spontaneous locomotion, anxiety, exploratory behavior, working memory, and spatial learning and memory.

As LC-NE activation is strongly linked to stress and anxiety[6,49], we first compared anxiety-like behavior in cre-expressing *Dbh*^{cre}, *Net*^{cre}, and *Th*^{cre} mice to their wild-type littermates. To this end, mice were left to freely explore an open field arena for 20 minutes (Fig. 5a, left)[50]. As mice show the intrinsic tendency to avoid open areas, the time spent near the walls of the arena serves as a proxy for anxiety, with less anxious mice spending more time in the center. While not all groups displayed significant avoidance of the arena center (p = 0.004 / 0.06 / 4 × 10^{-4} / 4 × 10^{-5} / 0.14 / 6 × 10^{-5} for *Dbh*^{cre} / *Dbh*^{WT} / *Net*^{cre} / *Net*^{WT} / *Th*^{cre} / *Th*^{WT}, respectively; one-sample t-test against chance level (16 %), n = 16 mice per group), anxiogenic conditions of the paradigm could be confirmed when pooling the data of all mice (p = 6 × 10^{-15}, n = 96 mice). When comparing 8 males and 8 females of each heterozygous cre-expressing line with a corresponding number of wild-type littermates of each mouse line, we did not detect any significant behavioral difference that could be explained by either genotype, sex, or the interactions of these two factors in any mouse line (Fig. 5a, right; two-way ANOVA; genotype effects: *scie*.45, p = 0.51; *Net*^{cre}: F_{28} = 0.54, p = 0.47; *Th*^{cre}: F_{28} = 0.01, p = 0.91; effects of sex and interactions of sex and genotype are shown in Supplementary table S2). Also, additional readouts used to approximate anxiety and spontaneous locomotion did not indicate any genotype-dependent behavioral difference in any mouse line (Fig. S10).

As an additional experiment approximating anxiety-related behavior, mice were left to explore an elevated plus maze (EPM)[51] for 5 minutes. The EPM consists of four arms radiating from a central platform, with two opposing arms being walled and the other two arms being open (Fig. 5b, left). Thus, mice need to balance their natural exploratory drive with the need to avoid exposed areas. At the start of the experiment, mice are placed on the central platform, and the time spent in the open and closed arms serves as a proxy for anxiety, with less anxious mice spending more time in the open arms. Again, significant avoidance of the open arms could not be demonstrated in each experimental group (p = 0.08 / 0.002 / 5 × 10^{-4} / 1 × 10^{-4} / 0.01 / 0.23 for *Dbh*^{cre} / *Dbh*^{WT} / *Net*^{cre} / *Net*^{WT} / *Th*^{cre} / *Th*^{WT}, respectively; one-sample t-test against chance level (48 %), n = 16 mice per group), but the anxiogenic nature of this paradigm could be validated when pooling the data of all mice (p = 3 × 10^{-12}, n = 96 mice). Also, in the EPM, we did not detect any behavioral difference that could be explained by either genotype, sex, or the interactions of these two factors in any mouse line (Fig. 5b, right; two-way ANOVA; genotype effects: *Dbh*^{cre}: F_{28} = 1.96, p = 0.17; *Net*^{cre}: F_{28} = 0.01, p = 0.93; *Th*^{cre}: F_{28} = 0.32, p = 0.57; effects of sex and interactions of sex and genotype are shown

in Supplementary table S2). Similarly, no behavioral alterations were found in any additional parameters extracted from the EPM (Fig. S11). In conclusion, we did not detect any genotype-related changes in anxiety-like behavior in any mouse line tested in two distinct experimental paradigms under light anxiogenic conditions.

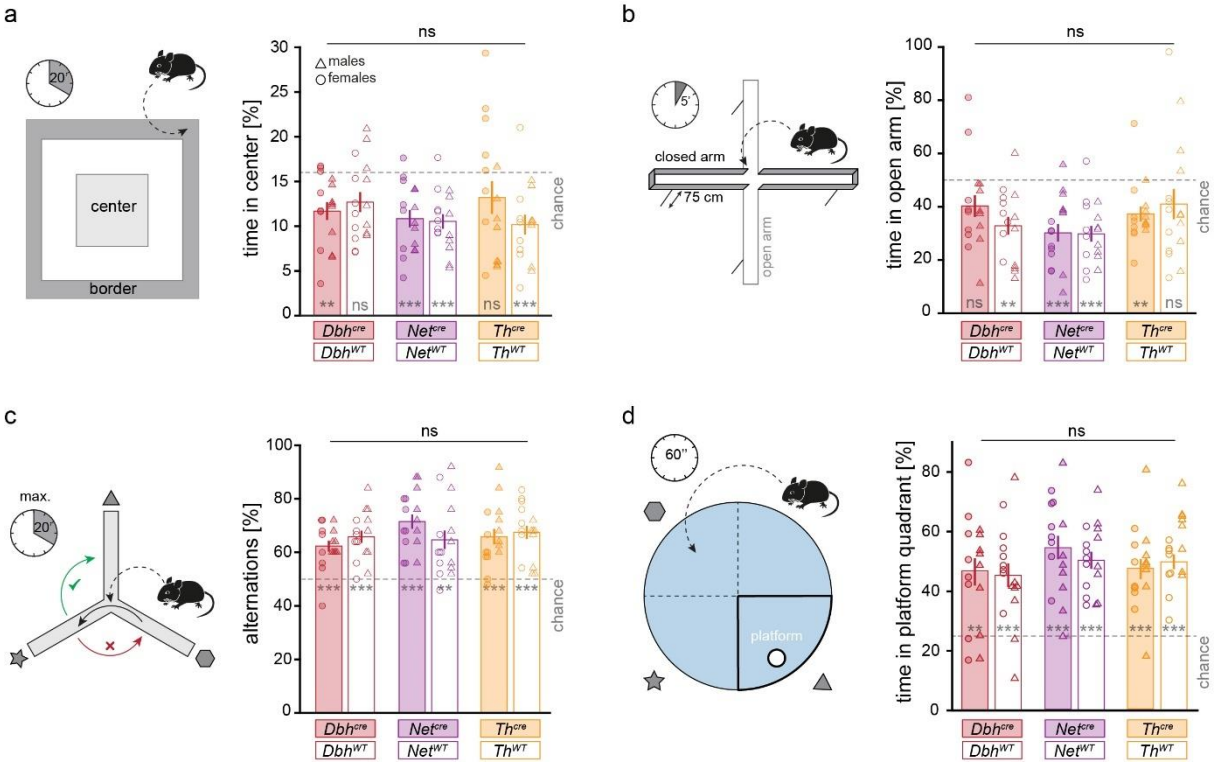

Figure 5 | Behavioral screening of cre-expressing mice. a, left: Mice were placed in one corner of the arena and left to explore the open field arena for 20 minutes. The time spent in the center of the arena approximates anxiety-like behavior. Right: The percentage of time spent in the center of the arena indicates no difference in anxiety-like behavior of cre-expressing mice (filled bars) as compared to wild-type littermates (empty bars) of different driver lines. **b**, left: Mice were placed on the central platform of the elevated plus maze and left to explore the maze for 5 minutes. The time spent in open arms of the maze approximates anxiety-like behavior. Right: The percentage of time spent in open arms indicates no difference in anxiety-like behavior of cre-expressing mice as compared to wild-type littermates in any driver line. **c**, left: Mice were placed in the center of the Y-maze and left to explore the maze until 26 transitions were made, for a maximum of 15 minutes. Upon the first transition between arms (black arrow), the next transition is expected to occur towards the previously unexplored arm (green arrow), rather than to the arm that was just visited before (red arrow). Right: The percentage of alterations (i.e., consecutive visits of all three arms) over the total number of transitions is above chance level (dashed line) in all groups, while no genotype-dependent differences in working memory were detected between cre-expressing mice and wild-type littermates in any mouse line. **d**, left: Mice are trained to find a hidden platform in a circular pool filled with opaque water on two consecutive days. On day three, the platform is removed, and the time spent in the area where the platform was previously located serves as a proxy for spatial memory. Right: the percentage of time spent in the platform quadrant was above chance level (dashed line) in all groups, while no genotype-dependent differences in spatial memory were detected between cre-expressing mice and wild-type littermates in any mouse line. All data is depicted as mean ± standard error of the mean. ns = not significant. **/*** for $p < 0.01/0.001$, respectively, tested against chance level. n = 8 females (circles) and 8 males (triangles). Numerical data underlying this figure can be found in supplementary material 1 (S1_Data.xlsx).

443 Recent studies have demonstrated the involvement of the LC-NE system in the
444 formation of episodic and spatial memory[52,53], which we investigated in two additional
445 experiments. First, we employed the Y-maze paradigm to approximate working memory in
446 mice. In this assay, mice are placed in a maze with 3 symmetrically radiating arms, which they
447 are free to explore. Based on the innate tendency to explore novel environments, mice
448 spontaneously alternate between arms, i.e. when leaving one arm, they tend to move to the
449 arm that was not previously visited, rather than the arm that was previously explored (Fig. 5c,
450 left; visual cues were given to distinguish the different arms)[54,55]. This was quantified as the
451 fraction of alternations (i.e., consecutive visits of all three arms) over the total number of
452 transitions. The fraction of alternations was above chance level in all groups ($p < 0.01$;
453 Bonferroni-corrected one-sample *t*-test), indicating intact working memory in all groups. No
454 genotype-related behavioral changes were found (Fig. 5c, right; two-way ANOVA; genotype
455 effects: Dbh^{cre}: $F_{28} = 1.23$, $p = 0.26$; Net^{cre}: $F_{28} = 2.48$, $p = 0.13$; Th^{cre}: $F_{28} = 0.23$, $p = 0.63$; effects
456 of sex and interactions of sex and genotype are shown in Supplementary table S2, additional
457 results from Y-maze experiments are shown in Fig. S12).

458 Finally, to investigate spatial memory formation, we performed the Morris Water
459 Maze (MWM) task[56]. In the MWM, mice are placed in a circular pool filled with opaque water
460 that contains a hidden platform placed just below to the surface that mice can access to
461 escape the water (Fig. 5d, left; visual cues for spatial orientation were placed around the pool).
462 The MWM task was performed on three consecutive days after habituating mice to the water.
463 On the first two days, each mouse was placed in the water four times, at pseudo-randomized
464 positions in each trial. Decreased latencies and travel distances to reach the platform during
465 these training sessions indicated successful spatial learning in all experimental groups (Fig.
466 S13). On the second day, after the first two training trials, a probe trial was performed, in
467 which the platform was removed. The time spent in the platform quadrant approximates
468 short-term memory. On day three, a single probe trial was done, from which long-term
469 memory can be measured. The time spent in the platform quadrant during the probe trial on
470 day 3 was above chance level in all groups ($p < 0.01$; Bonferroni-corrected one-sample *t*-test),
471 indicating intact spatial memory formation. No genotype-dependent behavioral changes were
472 found (Fig. 5d, right; two-way ANOVA; genotype effects: Dbh^{cre}: $F_{28} = 1.14$, $p = 0.29$; Net^{cre}:
473 $F_{28} = 0.56$, $p = 0.46$; Th^{cre}: $F_{28} = 0.34$, $p = 0.56$; effects of sex and interactions of sex and
474 genotype, as well as results of the short-term memory test on day two are shown in
475 Supplementary table S2, additional results of the MWM experiments on day 3 are shown in
476 Fig. S14). In conclusion, we found no genotype-related behavioral differences between cre-
477 expressing mice and wild-type littermates in Dbh^{cre}, Net^{cre}, or Th^{cre} mice in the four behavioral
478 assays considered.

479

480

481

482 *PRS×8-based constructs for monitoring and manipulating LC activity*

483 Transgene expression driven by the PRS×8 promoter, which has high efficacy and good local
484 specificity (Fig. 1), is independent of cre recombinase. Thus, molecular targeting of LC-NE
485 neurons with the PRS×8 promoter can be applied either to wild-type mice, eliminating the
486 need for a cre driver line, or to a different cre driver line, providing access to two genetically
487 distinct neuronal populations in the same animal[32]. In addition, PRS×8-based transgene
488 expression can be applied to different species, as demonstrated in rats[25,28,57,58]. As there are
489 currently very few AAV-carried PRS×8-based constructs available, we developed a set of
490 PRS×8-based constructs to enable the monitoring and control of LC-NE activity (of note, canine
491 Adenovirus type 2 (CAV-2) carrying PRSx8-mediated transgenes are commercially available at
492 https://plateau-igmm.pvm.cnrs.fr/?cat=69).

493 To optically monitor LC-NE activity, we developed a construct encoding jGCaMP8m[59]
494 under the control of the PRS×8 promoter. We directly compared its functionality to a
495 conditionally expressed indicator in the contralateral LC of the same animal. To do so, we
496 injected rAAV2/9-PRS×8-jGCaMP8m into one LC of a *Dbh*^{cre} mouse and a cre-dependent,
497 spectrally compatible calcium indicator jRGECO1a[60] (AAV2/1-hSyn-DIO-jRGECO1a) into the
498 contralateral LC (Fig. 6a-b). In line with our previous results (Fig. 1), we observed a specificity
499 of 92.5 % and an efficacy of 79.6 % for PRS×8-jGCaMP8m, and a specificity and efficacy of
500 94.9 % and 64.3 % for DIO-jRGECO1a. We then implanted optical fibers above the injection
501 sites and obtained fiber photometry recordings simultaneously from both LC of awake, head-
502 fixed mice, while monitoring the pupil diameter of the animals (Fig. 6c), observing strong
503 correlations between the neuronal dynamics of jGCaMP8m- and jRGECO1a-expressing LC (r =
504 0.73, $p > 0.0001$; Pearson's correlation coefficient for recording of 20 minutes duration). Since
505 the LC-NE system causally controls pupil-linked arousal[61], we aligned all signals to local peaks
506 of the derivative of the pupil diameter that occurred in the absence of locomotion (Fig. 6d),
507 as pupil dynamics and locomotion are tightly coupled in mice[62]. As expected, peaks in pupil
508 size were preceded by peaks in LC activity, which confirms the biological relevance of the
509 recorded signals. Importantly, similar temporal dynamics of LC activity were observed in both
510 channels, indicating that PRS×8- and *Dbh*^{cre}-mediated expression of calcium indicators reveals
511 comparable functional signals of LC activity.

512 Importantly, when exciting the calcium indicators at their quasi-isosbestic wavelength
513 (405 nm), no peaks were observed in either channel (Fig. 6e), confirming that the observed
514 peaks in fluorescence indeed resulted from calcium dynamics, and not from motion or
515 hemodynamic artefacts. Additional controls were performed to exclude spectral crosstalk of
516 the calcium indicators by restricting our recording from both LC either to the green or to the
517 red spectral range. When aligning signals to pupil dilation, the previously observed peak in
518 jRGECO1a fluorescence was not present in the green spectrum (Fig. 6f), and, vice versa, the
519 previously observed peak in PRS×8-jGCaMP8m fluorescence was abolished the red spectral
520 range (Fig. 6g), confirming absence of spectral crosstalk between the two indicators.

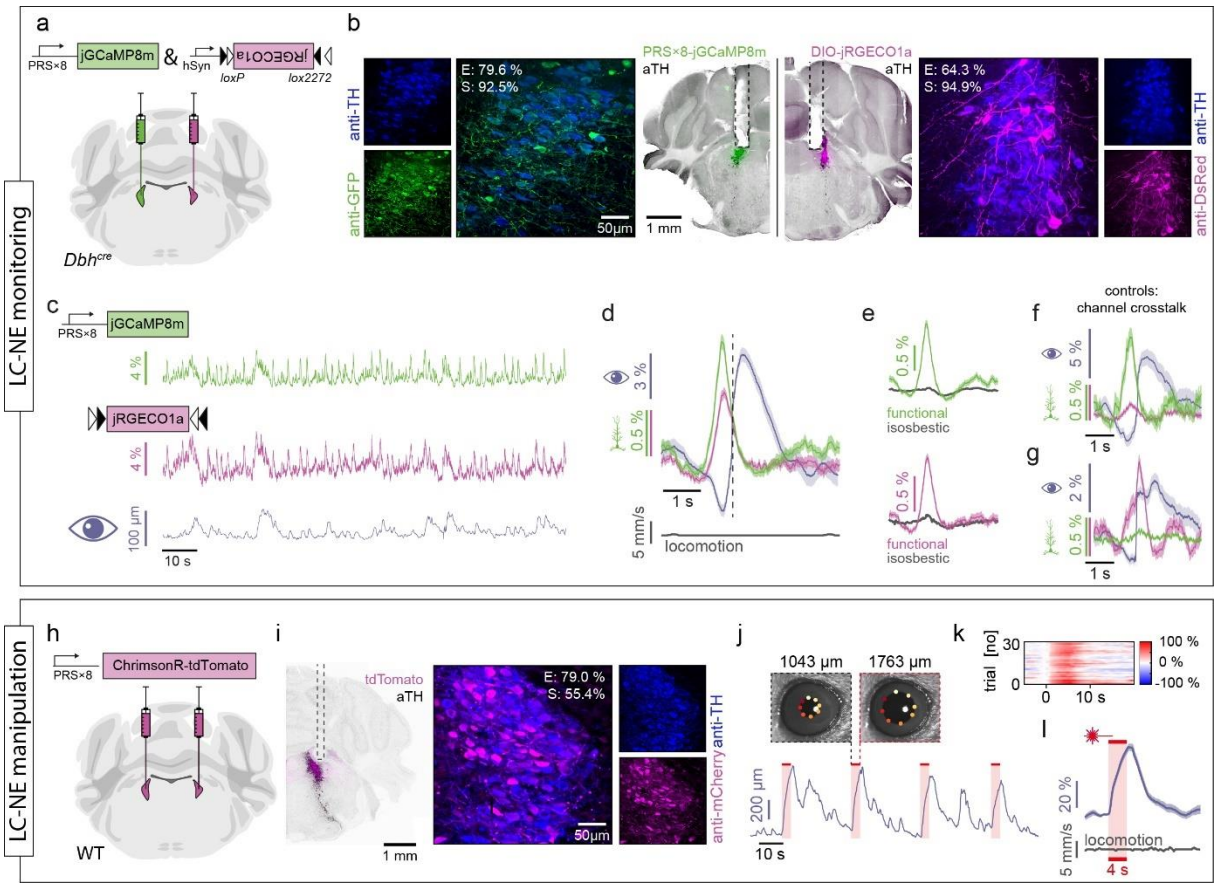

Figure 6 | PRSx8-mediated constructs to monitor and manipulate LC activity. a, PRS×8-jGCaMP8m was injected into one LC of a *Dbh*^{cre} mouse and DIO-jRGECO1a was injected in the contralateral LC. **b,** Epifluorescence images of hemi-brain slices expressing PRS×8-jGCaMP8m (green, left) and DIO-jRGECO1a (magenta, right). Immunostaining against TH is shown in black, while dashed lines indicate the optical fiber tracts. Confocal images with quantification of efficiency (E) and specificity (S) are shown in the channel-merged confocal images. **c,** Simultaneous fiber photometry recordings of PRS×8-jGCaMP8m fluorescence (top) and DIO-jRGECO1a fluorescence (center), along with the pupil diameter of the mouse (bottom). **d,** ΔF (mean ± standard error of the mean) of PRS×8-jGCaMP8m (green) and DIO-jRGECO1a (magenta) as well as pupil diameter (grey) locked to local peaks in the derivative of the pupil diameter (indicated by dashed line, *n* = 171 peaks from 20 minutes of recording). Only events in the absence of locomotion (grey, bottom) were analyzed. **e,** Pupil-aligned functional and isosbestic fluorescence of PRS×8-jGCaMP8m (top) and DIO-jRGECO1a (bottom). Functional excitation was done at 470 nm for jGCaMP8m and 560 nm for jRGECO1a, while isosbestic excitation for both indicators was done at 405 nm. **f,** ΔF of green-light-filtered PRS×8-jGCaMP8m (green) and DIO-jRGECO1a (magenta), locked to peaks in the derivative of pupil diameter, exclude major cross-talk from jGCaMP8m to the jRGECO1a channel (*n* = 52 peaks). **g,** ΔF of red-light-filtered PRS×8-jGCaMP8m (green) and DIO-jRGECO1a (magenta), locked to peaks in the derivative of pupil diameter, exclude major cross-talk from jRGECO1a to the jGCaMP8m channel (*n* = 84 peaks). **h,** Scheme of bilateral injections of PRS×8-ChrimsonR-tdTomato into the LC of a wild-type mouse. **i,** Epifluorescence image of a hemi-brain slice expressing PRS×8-ChrimsonR-tdTomato (left). tdTomato was amplified using a cross-reacting antibody against mCherry (magenta), while the LC was visualized with an anti-TH staining (black). Dashed lines indicate the fiber position (only the lesion caused by the fiber tip is visible in this slice). Transgene expression was quantified on confocal images (right). **j**, Pupil diameter of the mouse during bilateral optogenetic activation of the LC (red bars; 633 nm, ~5 mW, 20 ms pulses at 20 Hz for 4 seconds). Insets show DeepLabCut-traced videographic images at indicated time points before and after an optogenetic stimulus. **k**, Relative pupil diameter (color coded) during a recording session consisting of 30 trials with an inter-trial-interval of 30s. **l**, Pupil size in response to optogenetic stimulation (mean ± standard error of the mean across trials shown in k). Absence of locomotion is shown in grey (bottom).

547 Finally, we developed a construct encoding the red-light-sensitive cation channel
548 ChrimsonR[63] fused to tdTomato[64] under control of the PRS×8 promoter for optogenetic
549 activation of LC-NE neurons. After bilateral injection of rAAV2/9-PRS×8-ChrimsonR-tdTomato
550 (efficacy: 79.1 %, specificity: 55.4%,) and implantation of optical fibers above the LC in a wild-
551 type mouse (Fig. 6h-i), we illuminated the LC (633 nm) while monitoring the pupil (Fig. 6j). As
552 expected, illumination of the LC reliably induced pupil dilation, confirming functional
553 optogenetic activation of the LC by PRS×8-ChrimsonR-tdTomato (Fig. 6k, l). Importantly, pupil
554 dilations occurred in the absence of locomotion (Fig. 6l, grey), confirming direct pupil control
555 of the LC.

556

557 **Discussion**

558 The LC-NE system consists of a small number of neurons located deep in the brain stem. It is
559 responsible for the modulation of a wide range of body and brain functions. In recent years,
560 an increasing number of studies have used genetic strategies to selectively and specifically
561 target the LC-NE system. Importantly, the interpretation of these studies depends on the
562 reliability of transgene expression in this small cell population. However, a direct
563 quantification of these parameters is not always reported, and a direct comparison of these
564 model systems is lacking. In this study, we performed a side-by-side comparison of four
565 strategies for viral-based genetic manipulation of the mouse LC, encompassing LC
566 transduction with floxed transgenes in *Dbh*^{cre}, *Net*^{cre} and *Th*^{cre} transgenic driver lines, and
567 transgene expression under the control of a synthetic, NE-specific promoter (PRS×8).

568 Using immunohistological analysis, we found differences in both expression efficacy
569 and specificity between these model systems. *Dbh*^{cre} mice and *Net*^{cre} *mice* showed the highest
570 specificity and efficacy of transgene expression, with no significant differences between them.
571 In comparison, PRS×8 promoter-driven expression showed comparable efficacy to *Dbh*^{cre} *and*
572 *Net*^{cre} mice, but lower specificity compared to *Dbh*^{cre} mice. Conditional expression in *Th*^{cre} mice
573 — a transgenic line commonly used to target LC — showed both lower efficacy and specificity
574 than the other approaches. Finally, substantial ectopic transgene expression in regions distant
575 from the LC was observed, particularly with PRS×8- and *Th*^{cre}-mediated transgene expression.
576 Some regions, such as the parabrachial or the vestibular nucleus, frequently showed ectopic
577 expression. While we cannot exclude a molecular predisposition of these neurons to TH- or
578 PRS×8-mediated transgene expression, we propose a different reason: As both the
579 parabrachial and the vestibular nucleus also frequently expressed non-conditional
580 fluorophores (see Fig 4 or S9, especially upon injection of rAAV2/2 or low volumes of
581 rAAV2/9), these regions might simply be better accessible for the viral suspension, likely due
582 to the neuronal density in these regions, or due to the arrangement of nuclei and fiber tracts
583 in the brainstem.

584 It is important to note that TH-positive neurons have been reported in brain areas close
585 to the LC, such as the parabrachial nucleus[65]. Although the ectopic expression in our study was

586 not localized to these TH-positive neurons (as indicated by the absent TH co-staining), this
587 population should be kept in mind as it may lead to erroneous interpretations of the function
588 of LC-NE neurons if LC-specificity is taken for granted in *Th*^{cre} mice. Ectopic transgene
589 expression was much less pronounced in *Net*^{cre} mice, and only very low ectopic expression
590 was observed in *Dbh*^{cre} mice. In fiber photometry experiments that directly target the LC,
591 ectopic expression may be less of a concern because signals are typically recorded in close
592 proximity to the tip of the optical fiber[66,67], adding spatial precision to the molecular specificity
593 of transgene expression. By contrast, recordings in putative projection sites may get
594 contaminated by afferents from ectopically expressing neurons. In addition, in optogenetic
595 studies, where the intensity of activation light is typically chosen to be well above threshold,
596 light scattering could also lead to the activation of opsins ectopically expressed in tissue
597 distant the fiber tip.

598 As mentioned above, a direct side-by-side comparison of virus-mediated LC
599 transduction under comparable conditions (i.e., same viral titers, injection volumes, viral
600 serotypes, etc.) was missing. However, several different studies reported the transduction
601 efficiency and specificity individually for a given model system. In *Dbh*^{cre} mice, viral
602 transduction efficacies between 83% and 96% of *TH*-immunoreactive neurons have been
603 reported[68–70], with a specificity of 95%[69]. In *Net*^{cre} mice, an efficacy of ~99% was reported, with
604 no transgene expressing cells found outside of the LC[21]. However, it is important to note that
605 transgene expression in this study was not achieved by viral injections but by crossing *Net*^{cre}
606 mice with a reporter mouse line. With respect to PRS×8 promoter-mediated expression,
607 specificities between 95-98% were reported in mice, while efficacy was not quantified[26,27]. In
608 addition, a more recent study by Stevens et al.[44] reported efficacies ranging from ~50 to 90%,
609 with specificities between ~60 and 95% (depending on the volume and titer of the injected
610 virus). This study reported the best results with a titer of 1×10^{11} gc/ml (71-77% efficacy, ~96%
611 specificity). At higher titers (1×10^{12} gc/ml), specificity decreased to 60%. At even higher titers
612 (5-20 $\times 10^{12}$ gc/ml) the efficacy also decreased, and substantial toxicity was observed. The titer
613 used in our study (8×10^{11} gc/ml) comes closest to the 1×10^{12} gc/ml condition of Stevens et
614 al., and comparable efficacy (70-90%) and specificity (60-80%) were observed. Therefore, it is
615 likely that the specificity of PRS×8 driven expression can be improved in the future by using
616 lower titers. However, it is important to note that the majority of studies used PRS×8-driven
617 constructs in combination with recombinant adenoviruses[25] or CAV-2[26–28,44], which have a
618 different tropism and transduction efficacy than rAAV2/9 used in our study[71]. Considering
619 rAAV pseudotypes, insufficient PRS×8-mediated transgene expression was reported with
620 rAAV2/7[72] (~20.6 % efficacy), whereas robust expression was reported after injection of
621 rAAV2/9[43,58]. These findings highlight the importance of viral serotype and careful titration of
622 the viral titer when implementing the PRS×8 promoter for genetic manipulation of the LC.

623 In *Th*^{cre} mice, we show that cre-mediated expression only partially covers TH-positive
624 LC neurons. Low efficacy and ectopic, cre-dependent transgene expression were also
625 previously described in close proximity to the LC[22,73], the substantia nigra[22], the VTA[39,53], and

626 various brain regions not directly related to catecholaminergic signaling[23,39,74]. A detailed
627 study by Lammel and colleagues[39] reported specificities of 48 and 59% in the ventral
628 tegmental area of *Th*$^{IRES\text{-}cre}$ and *Th*^{cre} mice, respectively, which aligns well with the specificity
629 we observed in the LC. Higher efficacy and specificity for *Dbh*^{cre} when compared to *Th*^{cre} mice
630 was also reported for catecholaminergic neurons in the A1/C1 area of the brainstem, but
631 differences were not as pronounced as in our study[75]. Overall, our results are consistent with
632 previous findings from various different studies investigating cre-dependent expression in the
633 LC. Thus, our systematic comparison revealed marked differences in expression patterns of
634 cre driver lines and promoter-mediated transgene expression of the LC-NE system.

635 The observed differences in transgene expression patterns may be explained, at least
636 in part, by the different strategies used to generate different mouse lines: *Dbh*^{cre} mice were
637 generated using a knock-in/knock-out strategy, resulting in cre expression directly from
638 the *Dbh* locus. While this approach disrupts endogenous *Dbh* expression, the use of
639 heterozygous *Dbh*^{cre} mice allows for safe and specific cre expression with a low risk for
640 unwanted side effects. In contrast, the transgenic *Th*^{cre} mice were generated by random
641 insertion of a construct containing the *Th* promoter followed by a cre coding sequence. This
642 could explain leaky cre expression due to potential activity of other promoter elements in the
643 vicinity of the integration site. However, also different strategies for *Th*-specific cre-expression
644 yielded low specificity in the VTA – as shown for knock-in mice expressing Cre-recombinase
645 from the downstream-untranslated region of the endogenous Th gene via an internal
646 ribosomal entry sequence (IRES). The *Net*^{cre} mice (and other commonly used *Dbh*^{cre} and *Th*^{cre}
647 lines[16]) are bacterial artificial chromosome (BAC) transgenic mice generated by random
648 insertion of a BAC sequence containing the gene of interest and a cre coding sequence. The
649 inclusion of the gene increases the possibility of preserving key regulatory elements required
650 for accurate cell-type-specific expression, which are not included in the case of *Th*^{cre} mice or
651 when using the synthetic, minimal PRS×8 promoter. However, it is important to note that
652 regulatory elements are often distant from the promoter, and therefore incomplete and
653 ectopic transgene expression similar to traditional transgenic mice may also be found in BAC
654 transgenic mice[16]. Unpredictable ectopic expression may also be driven by transcriptional
655 regulatory elements of genes flanking the transgene insertion site. In addition, random
656 transgene insertion may interrupt endogenous genes, resulting in loss-of-function mutations
657 and unexpected phenotypes. These effects are avoided in targeted knock-in alleles, as was
658 used to generated the *Dbh*^{cre} mice. It is important to mention that additional *Th*^{cre} and *Dbh*^{cre}
659 mouse lines exist that have also been generated using BACs[18] and targeted mutations[23].
660 However, the use of these mice is much less widespread and there are currently no vendors
661 maintaining colonies of these lines.

662 Ectopic expression is not limited to the *Th* promoter, but has also been reported in a
663 wide variety of model systems, including cholinergic and catecholaminergic cells of the
664 retina[76,77], dopaminergic cells of the dorsal raphe nucleus[78] and the limbic system[79], and
665 somatostatin-expressing interneurons[80] and microglia[81] in the cerebral cortex. Such ectopic

666 expression may result from promoters that are weakly active, leading to low levels of native
667 protein expression, which may not be functionally relevant. Similarly, low expression levels of
668 a direct reporter, such as a fluorophore in a reporter mouse line, may not be a major concern
669 because the detected signal may be much weaker compared to true positive cells exhibiting
670 high activity of the promoter of interest. However, in cre-reporter line, even low levels of cre
671 are sufficient to recombine floxed transgenes over time, leading to substantial expression of
672 the transgene and thus uncoupling of endogenous cre expression levels from cre-dependent
673 transgene expression[82,83]. This explanation is consistent with reports from homozygous Ai32
674 reporter mice where immunostainings revealed leaky channelrhodopsin-2 expression
675 throughout the brain in the absence of cre, but at levels insufficient to induce detectable
676 photocurrents[84]. Other explanations for ectopic expression include legitimate but transient
677 promoter expression during development[23,30,31,39,83], changes in endogenous expression
678 patterns resulting from transgene integration itself[76], or recombination of cre in the
679 germline[83].

680 Phenotypic alterations have been previously reported for different cre driver lines to
681 access the cholinergic (*Chat*^{cre})[46] and dopaminergic systems (*Dat*^{cre}, *Dat*^{IREScre}, and *Th*^{cre} upon
682 amphetamine application)[47,48]. Therefore, we performed a behavioral screening sensitive to
683 anxiety-like behaviors as well as learning and memory, all of which have been linked to LC
684 function. We found no genotype-related effect on spontaneous locomotion, anxiety,
685 exploratory behavior, working memory, and spatial learning and memory. These results are
686 particularly relevant for the *Dbh*^{cre} line, because the knock-in/knock-out design of this mouse
687 line disrupts endogenous *Dbh* expression in one allele of heterozygous animals. This approach
688 could lead to reduced levels of norepinephrine while accumulating its precursor molecule
689 dopamine, and consequently disrupting behavior. Furthermore, we did not observe any sex-
690 related effects on anxiety-like behavior, which is in contrast to a recent study reporting higher
691 levels of anxiety in female mice using the open field and elevated plus maze paradigms[85].
692 While sex differences in the EPM were confirmed by one additional study[86], two studies
693 reported the absence of sex effects on anxiety-like behavior using the open field test[86,87].
694 These discrepancies may be explained (in part) by the estrous cycle, which is linked to *Th*
695 transcription[88]. It has been demonstrated that mice in the proestrus and estrus stages showed
696 increased anxiogenic behavior, while mice in other stages were comparable to males[85]. As the
697 stage of the estrous cycle was not controlled in our experiments, experimental groups
698 randomly composed of females in different estrous cycles may have masked sex-dependent
699 effects in our experiments. Further factors that have been shown to influence the outcome of
700 these experimental paradigms are the sex of the experimenter[89,90], the history of handling[91,92],
701 as well as non-explicit factors of the laboratory itself[93,94]. In conclusion, our results suggest
702 that all mouse lines investigated here can be used equally, at least for the behavioral assays
703 we have included. However, caution should be exercised when extrapolating these results to
704 other experimental paradigms such as instructed behavior or experimental conditions that
705 differ substantially from those we used.

706 We show that *Dbh*^{cre}, *Net*^{cre}, and PRS×8-mediated transgene expression provides
707 reliable access to the LC-NE system. In parallel, we did not observe any genotype-related
708 behavioral changes in any mouse line. Apart from these aspects, additional factors should be
709 considered when deciding which LC-targeting strategy to use. First of all, *Dbh*^{cre} and *Net*^{cre}
710 mice showed the highest specificity. Second, the cre-lox system is widely established.
711 Therefore, cre driver lines can be easily combined with off-the-shelf viral constructs that are
712 readily available from public commercial and non-commercial repositories. Finally, driver lines
713 can be crossed with various reporter lines, allowing reproducible transgene expression
714 without the need for stereotactic surgery. Of note, *Dbh*^{cre} mice are commercially available in
715 public repositories, making them available to the scientific community, while a material
716 transfer agreement is required to obtain *Net*^{cre} mice. In contrast, PRS×8-based transgene
717 expression is possible in wild-type mice and, therefore, no transgenic mouse line colonies are
718 required. This not only eliminates the risk of mouse-line-dependent phenotypic effects that
719 we may have missed, but also facilitates easy and straightforward access to the LC-NE system.
720 Moreover, it reduces the number of excess animals that can result from unwanted genotypes
721 when breeding a particular mouse line. In addition, PRS×8 allows a high degree of flexibility
722 for manipulation and readout of different molecularly defined circuits when combined with
723 cre lines other than those related to the noradrenergic system[32]. Finally, the PRS×8-system
724 can be implemented in species other than the mouse, as recently demonstrated in the rat[28].

725 Care should be taken when translating our findings to other model systems, such as
726 rats, where other approaches than those reported in this study are also available. For example,
727 transgene expression mediated by the PRS×8 promoter resulted in an efficacy of 83% of TH^+
728 neurons[28] at a specificity of 97-100% in this model system[25,28,58]. While this efficacy is in line
729 with our findings, the reported specificities exceed the ones of our experiments, which might
730 be due to the injected titers (as discussed above)[44] or the serotype, as many studies in rats
731 relied on CAV-2 instead of AAVs[28,44]. Furthermore, *Th*^{cre} transgenic rats have been created over
732 a decade ago[24] and a specificity of 97-100 % was reported for viral transduction of the LC-NE
733 system, while efficacy amounted to 73-75 %[24,95]. Most recently, a novel *Dbh*^{cre} rat line has
734 been created and characterized with both high specificity (97-99 %) and efficacy (95-98 %)[20],
735 thereby offering one more approach to target the LC-NE system in rats with high precision.
736 However, regardless of the model system chosen, our study highlights the importance of
737 rigorous post-mortem verification of viral transduction and the implementation of
738 appropriate controls for each system.

739 It is also important to consider viral titers and pseudotypes when extrapolating our
740 conclusions to different experimental settings. First, we relied on a single viral titer in all model
741 systems. While all experimental groups were injected with the same amount of virus, it has
742 been shown that efficacy, specificity, and potential toxicity of PRS×8-mediated gene
743 expression are dependent on the viral titer[44]. Similarly, the specificity of cre-dependent
744 transgene expression is dependent on the viral titer[96,97]. Therefore, it may well be that greater
745 efficacy and specificity of gene expression could be achieved when optimizing the viral titer

746 for a specific application. In addition, the majority of our experiments was performed with
747 rAAV2/9, and, therefore, may not be generalizable to other serotypes or even different virus
748 families. For example, an rAAV pseudotype with less broad tropism than rAAV2/9 (e.g.,
749 rAAV2/2)[42] may lead to reduced ectopic expression and, therefore, higher apparent
750 specificity. Conversely, lower efficacy may be observed, if viral transduction of noradrenergic
751 neurons is limited due to low tropism of virus.

752 Another consideration relates to the choice of antibodies for the detection of
753 transgene expression and cell identity. For example, we have broadly stained against tyrosine
754 hydroxylase while anti-DBH or anti-NET antibodies could have been used to exclusively detect
755 noradrenergic neurons. However, all of our experimental groups were stained with the same
756 antibody, and the outcome of our study did not favor the *Th*^{cre} line.

757 In conclusion, we present a quantitative side-by-side comparison of four different
758 strategies to genetically access the mouse LC, resulting in heterogeneous patterns of
759 transgene expression. These findings may assist in the design of future studies and in the
760 interpretation of results obtained from previous studies using any of these model systems.
761 For example, a recent study described micro-arousals, but no sustained wake episodes upon
762 optogenetic LC activation in *Dbh*^{cre} mice, whereas sustained wake episodes were evoked by
763 optogenetic LC activation in *Th*^{cre} mice[73]. One possibility is that this discrepancy could be the
764 consequence of different neuronal populations targeted in each line, and highlights the
765 importance of selecting an appropriate model system. In addition to the analysis of transgene
766 expression patterns, we developed AAV-based tools relying on the PRS×8 promoter for
767 marking, monitoring, and manipulating LC-NE neurons, thereby increasing experimental
768 flexibility and facilitating the investigation of the LC-NE system in various genetic backgrounds.
769 Taken together, our results contribute to the design of more refined studies and thus to a
770 deeper understanding of the heterogeneous functionality of the LC-NE system in the future.

771

772

773 **Material and Methods**

774 *Ethics statement.* All experiments were performed in compliance with German law according
775 to the directive 2010/63/EU of the *European Parliament* on the protection of animals used for
776 scientific purposes and in accordance with the 3R principles. Procedures were approved by
777 local animal care committees (*Behörde für Gesundheit und Verbraucherschutz*, Hamburg,
778 Germany: N033/2019; *Regierungspräsidium Karlsruhe*, Germany: 35-9185.81/G-213/22).

779 *Animals.* Experiments were performed on adult (2-6 months of age) C57BL/6J, *Th*^{cre}[22], *Net*^{cre}[21]
780 and *Dbh*^{cre}[19] mice, housed in cages with nesting material with no more than 5 animals per cage
781 at the animal facility of the *Center for Molecular Neurobiology* of the *University Medical Center*
782 *Hamburg-Eppendorf* or at the *Medical Faculty Mannheim of the University of Heidelberg*.

783 Animals were kept in a 12/12 h light/dark cycle, at 20-24°C and 40-65% humidity, with access
784 to water and food ad libitum.

785 *Molecular biology.* The double-floxed inverted open reading frame variant for cre
786 dependent expression of *eGFP*[98] was created by cloning *eGFP* in antisense direction, flanked
787 by two loxP and lox2272 sites, behind the CAG promoter into an AAV2 backbone. PRS×8-based
788 constructs were created by cloning the respective transgene behind 8 repetitions of a de novo
789 synthetized Phox2a/Phox2b response site (PRS; based on the only PRS×8 construct (#89539)
790 available from *AddGene* at the time this study started) into an AAV2 backbone. PRS×8
791 constructs were generated for the expression of the green light emitting reporter protein
792 *eGFP*[98] (pAAV-PRS×8-eGFP; *AddGene* #192589), the green light emitting calcium indicator
793 jGCaMP8m[59] (pAAV-PRS×8-jGCaMP8m; *AddGene* #210400), and the red-light sensitive cation
794 channel ChrimsonR coupled to the red light emitting reporter protein tdTomato[63] (pAAV-
795 PRS×8-ChrimsonR-tdTomato; *AddGene* #192587). DNA was then packed into recombinant
796 adeno-associated virus serotype 2/9 (rAAV2/9) at the vector core facility of the *University*
797 *Medical Center Hamburg-Eppendorf*, Germany, or by *VectorBuilder*.

798 *Stereotactic injections and fiber implantation*. For surgical procedures, mice were
799 either anesthetized with Midazolam/Medetomidine/Fentanyl (MMF; 5/0.5/0.05 mg/kg
800 bodyweight in NaCl, intraperitoneal), or with Isoflurane (5% for induction, ~1.5% for
801 maintenance). In the case of isoflurane anesthesia, adequate analgesia was achieved with
802 buprenorphine (0.1 mg/kg in NaCl, intraperitoneal). After confirming anesthesia and analgesia
803 by the absence of the paw withdrawal reflex, the head was shaved with a fine trimmer and
804 sterilized with iodine (*MundiPharma*). Mice were then fixed with an auxiliary ear bar (EB-6,
805 *Narishige Scientific*) in a stereotactic frame and positioned on a heating blanket to maintain
806 body temperature. Eyes were covered with an eye ointment (*Vidisic*, *Bausch + Lomb*) to avoid
807 drying. Subsequently, the scalp was opened (~1 cm incision) and the skull was cleaned with
808 NaCl (0.9%; *Braun*) and a bone scraper (*Fine Science Tools*). Bregma and lambda were
809 identified and stereotactically aligned. A small craniotomy was then performed above the
810 locus coeruleus (AP: –5.4; ML: ±0.9; DV: –3.6 mm relative to bregma; for later injections, the
811 mediolateral coordinates were changed to ±1.1 mm, see Fig. 4) using a dental drill (*Foredom*),
812 and was constantly kept moist to prevent drying.

813 The viral suspension was drawn into a borosilicate glass pipette (pulled from 0.2 mm
814 glass capillaries with a PC-100 puller; *Narishige*) using negative air pressure. 300 nl of titer-
815 matched (8×10^{11} gc/ml) viral suspension containing rAAV2/9 carrying DNA encoding *eGFP*
816 either in a cre-dependent (double-floxed inverted reading-frame, DIO) manner under control
817 of the CAG promoter (in the case of Dbh^{cre}, Net^{cre} and Th^{cre} animals) or unconditional under
818 control of the PRS×8 promoter (in the case of C57BL/6J mice) were bilaterally injected into the
819 LC with an injection speed of ~100 nl/min using a custom-made, air-pressure driven injection
820 system for the analysis of transgene expression in the different model systems. For viral
821 transduction of the VTA, 200 nl of virus suspension were injected at four different injection

822 sites (AP: -3.2; ML: ± 0.3; DV: -3.5 mm and AP: -3.2; ML: ± 0.5; DV: -3.2 mm relative to Bregma).
823 For investigations of promoter effects, 300 nl of rAAV2/9 carrying DNA encoding eGFP in a
824 cre-dependent manner under control of the human synapsin (hSyn) promoter were injected
825 in *Dbh*^{cre} mice at a titer of (8.2×10^{12} gc/ml). For investigating the effects of viral serotype and
826 injection volume on viral spread, 300 nl of rAAV2/2 and 300/100/50 nl of rAAV2/9 carrying
827 DNA encoding eGFP under control of the hSyn promoter were injected in wild-type mice in a
828 titer-matched manner at 6.8×10^{12} gc/ml. Injections of rAAV2/9-Ef1a-DO-DIO-tdTomato-eGFP
829 (2.3×10^{13} gc/ml; *AddGene* plasmid #37120)[45] into the LC were performed in *Dbh*^{cre}, *Net*^{cre} and
830 *Th*^{cre} animals. For fiber photometry experiments, we injected rAAV2/9-PRS×8-jGCaMP8m
831 (3×10^{12} gc/ml) and rAAV2/9-hSyn-DIO-jRGeco1a (2×10^{13} gc/ml) into the LC of a *Dbh*^{cre}
832 mouse. For optogenetic manipulation of the LC, 300 nl of rAAV2/9-PRSx8-ChrimsonR-
833 tdTomato (1×10^{12} gc/ml) were injected into each LC of a wild-type mouse. After virus
834 injection, the glass micropipette was kept in place for at least 5 min to avoid unnecessary viral
835 spread and was then slowly withdrawn. In the case of histological experiments, the skin was
836 closed with simple interrupted sutures and covered with iodine. In the case of fiber
837 photometry experiments, optical fibers (R-FOC-BL400C-50NA: 400 µm diameter, 0.5NA; *RWD*)
838 were inserted at AP: –5.4; ML: ±1.0; DV: –3.5 mm relative to bregma using a stereotactic
839 micromanipulator. For optogenetic experiments, optical fibers (R-FOC-BL400C-37NA: 200 µm
840 diameter, 0.37 NA; *RWD*) were inserted at the same coordinates. Fiber implants and a metal
841 headpost (00-200 500 2110; *Luigs & Neumann*) for animal fixation during the experiment were
842 fixed to the roughened skull using cyanoacrylate glue (Pattex; Henkel) and dental cement
843 (Super Bond C&B; *Sun Medical*). The incised skin was then glued to the dental cement to close
844 the site, before it was covered with iodine. Mice received analgesia (Carprofen; 4 mg/kg
845 bodyweight, subcutaneous), and Atipamezole/Flumazenil/Buprenorphine (FAB) was
846 administered (2.5/0.5/0.1 mg/kg bodyweight, intraperitoneal) to antagonize anesthesia in the
847 case of MMF; Isoflurane anesthetized mice were simply removed from the Isoflurane. For
848 recovery, mice were placed in a cage which was placed on a heating pad. Meloxicam was
849 mixed with soft food for the following two days.

850 *Tissue collection*. For perfusions, mice were deeply anesthetized with
851 Ketamine/Xylazine (180/24 mg/kg bodyweight, intraperitoneal), which was confirmed by the
852 absence of the paw withdrawal reflex. Mice were fixed on a silicone pad and transcardially
853 perfused with ~50 ml of phosphate buffered saline (PBS) to rinse out the blood and
854 subsequently with ~50 ml of 4% paraformaldehyde (PFA; pH 7; *Carl Roth GmbH*) to fix the
855 tissue. Brains were explanted and post-fixed in 4% PFA for at least 24h. After fixation brains
856 were embedded in 3% agarose (*Genaxxon Bioscience*) and coronal slices of ~50 µm thickness
857 were obtained using a vibratome (VT 1000S, *Leica*). Slices were stored in PBS at 4°C until they
858 were stained and mounted on microscope slides.

859 *Immunohistochemistry.* To block unspecific binding sites for antibodies, brain slices
860 were incubated in 10% normal goat serum (NGS) and 0.3-0.5% Triton X-100 in PBS for 2h at
861 room temperature. Slices were then incubated for two days at 4°C in a carrier solution (2%

862 NGS, 0.3-0.5% Triton X-100, in PBS) containing primary antibodies (see below) to allow for
863 sufficient target protein-primary antibody interaction. Subsequently, slices were rinsed 3
864 times for 5-10min in PBS to remove unbound primary antibodies. Following the washing steps,
865 slices were incubated with secondary antibodies (see below) in the above-mentioned carrier
866 solution over night at 4°C. Washing steps were repeated as described before in order to
867 remove unbound secondary antibodies. Finally, slices were mounted on microscope slides
868 using *Fluoromount* mounting medium (*Serva*, Germany).

869 To analyze eGFP expression in TH^+ cells of the LC (Fig. 1, Fig. 2, Fig. 3a-d, Fig. S1, Fig. S4,
870 Fig. S6, Fig. S8), slices were incubated with primary antibodies against tyrosine hydroxylase
871 (1:1000; AB152; *Invitrogen*, *Thermo Fisher Scientific*) derived from rabbit and against green
872 fluorescent protein (1:750; A10262; *Invitrogen*, *Thermo Fisher Scientific*) derived from chicken,
873 while Alexa Fluor 546 goat anti-rabbit (1:1000; A11035; *Invitrogen*, *Thermo Fisher Scientific*)
874 and Alexa Fluor 488 goat anti-chicken (1:1000; A11039; *Invitrogen*, *Thermo Fisher Scientific*)
875 secondary antibodies were used. To analyze the difference of natively expressed eGFP
876 fluorescence and antibody-stained eGFP fluorescence (Fig. S7), slices were incubated with a
877 primary antibody against green fluorescent protein (1:750; A10262; *Invitrogen*, *Thermo Fisher*
878 *Scientific*) derived from chicken and an Alexa Fluor 546 goat anti-chicken secondary antibody
879 (1:1000; A11040; *Invitrogen, Thermo Fisher Scientific*). In DO-DIO-experiments (Fig. 4), slices
880 were incubated with primary antibodies against tyrosine hydroxylase (1:1000; AB152;
881 *Invitrogen*, *Thermo Fisher Scientific*) derived from rabbit and against green fluorescent protein
882 (1:750; A10262; *Invitrogen*, *Thermo Fisher Scientific*) derived from chicken, while Alexa Fluor
883 647 goat anti-rabbit (1:1000; A32733; *Invitrogen*, *Thermo Fisher Scientific*) and Alexa Fluor 488
884 goat anti-chicken (1:1000; A11039; *Invitrogen*, *Thermo Fisher Scientific*) secondary antibodies
885 were used. No staining was performed against tdTomato. To visualize jGCaMP8m in TH^+
886 neurons of the LC (Fig. 6b), slices were incubated with primary antibodies against tyrosine
887 hydroxylase (1:1000; AB152; *Invitrogen*, *Thermo Fisher Scientific*) derived from rabbit and
888 against green fluorescent protein (1:500; A10262; *Invitrogen*, *Thermo Fisher Scientific*) derived
889 from chicken, while Alexa Fluor 647 goat anti-rabbit (1:1000; A32733; *Invitrogen*, *Thermo*
890 *Fisher Scientific*) and Alexa 488 goat anti-chicken (1:1000; A11039; *Invitrogen*, *Thermo Fisher*
891 *Scientific*) were used as secondary antibodies. To visualize jRGeco1a in TH^+ neurons of the LC
892 (Fig. 6b), slices were incubated with primary antibodies against tyrosine hydroxylase (1:500;
893 Cat. No. 213 104; *Synaptic Systems*) derived from guinea pig and against DsRed (1:500; Cat.
894 No. 632496; *TaKaRa Bio*) derived from rabbit, while Alexa Fluor 647 goat anti-guinea pig
895 (1:200; A21450; *Invitrogen*, *Thermo Fisher Scientific*) and Alexa 546 goat anti-rabbit (1:1000;
896 A11035; *Invitrogen*, *Thermo Fisher Scientific*) were used as secondary antibodies. To visualize
897 ChrimsonR-tdTomato in TH^+ neurons of the LC (Fig. 6i), slices were incubated with primary
898 antibodies against tyrosine hydroxylase (1:1000; AB152; *Invitrogen*, *Thermo Fisher Scientific*)
899 derived from rabbit and against mCherry (1:500; Cat. No. 632543; *TaKaRa Bio*) derived from
900 mouse, while Alexa Fluor 488 goat anti-mouse (1:1000; A32723; *Invitrogen*, *Thermo Fisher*

901 *Scientific*) and Alexa Fluor 647 goat anti-rabbit (1:1000; A32733; *Invitrogen*, *Thermo Fisher*
902 *Scientific*) were used as secondary antibodies.

903 *Image acquisition.* Confocal images of the LC were acquired in a Z-stack (2 µm step
904 size) using an LSM 900 airyscan 2 microscope (*Zeiss*, Germany), controlled by the *ZEN* 3.1
905 imaging software, with laser intensities and gain of the photomultiplier tubes adjusted to
906 maximize dynamic range while avoiding saturation of images. A Plan-APOCHROMAT 20X/0.8
907 objective was used, resulting in a field of view of 319.45 × 319.45 µm with a resolution of at
908 least 1744 × 1744 pixels (183.2 nm/pixel). Some images were taken at a resolution of
909 2044 × 2044 pixels (i.e., 0.156 nm/pixel), and subsequently down-sampled to match the
910 resolution of 1744 × 1744 pixels. Whole slices were either imaged using a *Zeiss AxioObserver*
911 epifluorescence microscope (*Zeiss*, Germany) with a Plan-APOCHROMAT 20×/0.8 objective,
912 controlled by the *ZEN* 3.3 imaging software (ectopic transgene expression: Fig. 2 and Fig. S8,
913 verification of LC transduction: Fig. 4, leakage of viral transduction: Fig. S4) or using a *Zeiss*
914 *Axio Scan Z.1* epifluorescence microscope (*Zeiss*, Germany) with a Plan-APOCHROMAT
915 20×/0.8 objective, controlled by the ZEN 3.1 imaging software (viral spread: Fig. 3 and Fig. S9).
916 *ImageJ*[99] was used to adjust image brightness, contrast, and create maximum intensity Z-
917 projections.

918 *Image analysis. Transgene expression* was detected at the cellular level using the deep-
919 learning-based algorithm *CellPose*[35]. In a first run, we analyzed all images from all approaches
920 semi-automatically (i.e., automatically segmented cells were manually curated). We then used
921 the obtained cell masks to re-train *CellPose*[36] in order to adapt it to our dataset. We have
922 uploaded this custom trained CellPose model, named "CP4LC_Wissing_Eschholz_et_al" as
923 supplementary material 2. In the second run, we used the re-trained model for automatic cell
924 segmentation without any manual annotation. Segmentation was done separately for each
925 channel, resulting in a total of 2766/3638/2774/2699 TH^+ cells and 2293/4195/1861/3061
926 $eGFP^+$ cells in Dbh^{cre}, Net^{cre}, Th^{cre}, and PRS×8-animals respectively (33/39/31/30 brain slices;
927 11/12/11/10 transduced LC; n = 7/7/7/7 mice). Please note that in our study transgene
928 expression of calcium indicators and optogenetic tools were harder to quantify in an
929 automated way, as transgene expression was not as bright and hence the delineation of
930 individual cells not as clear as compared to the expression of eGFP. The average number of
931 TH^+ cells that were found per slice was 83.8 ± 19.3, 93.3 ± 15.7, 89.5 ± 16.0, and 90.0 ± 15.3
932 cells (mean ± standard deviation) for Dbh^{cre}, Net^{cre}, Th^{cre}, and PRS×8, respectively. Cell
933 detection was cross-validated with quantification by two different experimenters, who
934 counted stained cells with the cell counter function of *ImageJ*. Cell masks of segmented cells
935 in the *eGFP* and *TH* channels exported from *CellPose* as .txt-files where then checked for
936 overlap using custom-written *MATLAB* scripts (*The MathWorks*; see data availability
937 statement). For quantification of transduction efficacy, co-expression was checked based on
938 the cell masks in the *TH* channel, and masks which had an overlap of ≥ 50% with the masks in
939 the *GFP* channel were defined as co-expressing. Similarly, co-expression was quantified based
940 on the cell masks in the *GFP* channel, in order to quantify the specificity of transduction. The

941 number of TH$^+$, *GFP*$^+$, and *TH-GFP*-co-expressing cells was subsequently summed up per
942 animal, in order to avoid biasing the results based on (i) the different amount of *TH*$^+$ cells on
943 individual slices and (ii) the total amount of slices taken from each animal (some slices had to
944 be excluded due to tissue damage during the mounting process). Quantification of the effect
945 of anti-*GFP* immunostaining on cell fluorescence was performed by fitting (least-squares) a
946 binormal model of the form $f_R = \phi(\text{bias} + \text{gain} \times \phi^{-1}(f_G)) + \varepsilon$ with $\varepsilon \sim N(0,\sigma^2)$; and where f_R and
947 f_G denotes the fluorescence in the red (*GFP*-stained) and green (native *eGFP*) channels
948 respectively, and ϕ corresponds to the normal cumulative distribution function. Comparisons
949 between the two channels have been performed based on the cell masks detected in the *GFP*-
950 stained channel, as we aimed to reveal additional cells upon *GFP* staining, which, by definition,
951 are not detected in the native *eGFP* channel. To quantify v*iral spread*, images were down-
952 sampled to 25 % of their original size using bicubic interpolation (MATLABs built-in function
953 *imresize*) and smoothed using a 2D gaussian filter with a kernel width of 50 µm (*imgaussfilt*)
954 before fluorescence was normalized from 0 to 1. Afterwards, viral spread was defined as
955 cumulative areas of the image in which fluorescence exceeded a certain threshold, while
956 thresholds were varied between 0 and 1 at an increment of 0.1.

957 *Behavioral screening.* All behavioral experiments were performed in a quiet, darkened
958 room by the same (female) experimenter, blind to the animal's genotype. Animals (genotype-
959 , age- and sex-matched littermates, max. 2 animals of the same genotype and sex per litter)
960 between 12 and 15 weeks of age at the start of the experiment were handled for 5 minutes
961 (manually picked up and let to freely explore the experimenter's hands and arms) every other
962 day in order to habituate mice to the experimenter. All experiments were video-recorded with
963 a regular (when experiments were performed under illumination) or an infrared camera
964 (when experiments were performed in darkness). All reported measures were performed
965 using the software *Ethovision* XT17 (*Noldus*, Netherlands), unless stated otherwise. *Open Field*
966 *Test.* An open field arena of 50 × 50 × 40 cm, homogeneously illuminated with white light of
967 25 lux, was used. At the start of the experiment, mice were placed in one corner of the box,
968 and their movement was tracked for the following 20 minutes. The time spent in the center
969 (the central 20 × 20 cm) and borders (5 cm from the walls) of the arena, the number of center
970 crossings, and the latency to enter the arena center for the first time served as proxies for
971 anxiety-like behavior, while the total travel distance served as a proxy for spontaneous
972 locomotion. *Elevated Plus Maze*. The elevated plus maze consisted of four arms (30 × 5 cm)
973 radiating from a central platform (5 × 5 cm), elevated 75 cm from the ground. Two opposing
974 arms are covered by opaque walls (height: 17 cm), while the two other arms remain open.
975 Mice were placed on the central platform and left to explore the maze for 5 minutes in total
976 darkness. The time spent on opened versus closed arms, the number of entries to open arms,
977 the fraction of open arm entries upon which mice went to the distant edge of the exposed
978 arm, and the latency to leave the center of the maze served as proxies for anxiety-like
979 behavior. In addition, the number of rearing events, the latency to the first rearing event, and
980 the percentage of time spent grooming served as indirect measure for the absence of anxiety.

981 EPM data acquisition and analysis were performed using *Observer* XT11 (*Noldus*,
982 Netherlands). *Y-maze*. The maze consisted of three symmetrically radiating arms (34 × 5 cm),
983 surrounded by walls (height: 30 cm) made of transparent plastic, with spatial cues placed
984 behind each wall, homogeneously illuminated with white light of 10 lux. Mice were placed in
985 the center of the maze and left to explore the maze until 26 transitions (entry to one arm with
986 all four paws) between neighboring arms were made, or for a maximum of 15 minutes.
987 Entering an arm after having visited the two other arms before, that is entering all three arms
988 of the maze in one sequence, was considered a complete alternation. The fraction of
989 alternations over all transitions (a proxy for working memory) as well as the time per transition
990 (a proxy for exploratory behavior) was manually extracted. *Morris Water Maze*. The water
991 maze consisted of a circular pool (diameter: 145 cm) filled with opaque water (19-21°C) with
992 non-toxic white paint, surrounded by black curtains, and homogeneously illuminated with
993 white light of 60 lux. A platform (diameter: 14 cm) was placed 1 cm below the water surface
994 in one of the four quadrants of the maze. Four landmarks (35 × 35 cm) of different shapes and
995 grey tones were placed on the walls of the maze to allow for orientation. Animals were
996 familiarized with swimming, platform searching, and handling in a pre-training session using a
997 small, rectangular water-tank. Mice had to search for a platform in three trials (10-20 minutes
998 inter-trial intervals), with a different platform location each time. Animals were transferred
999 back to their home cage, where heat lamps were provided. On training day 1 and 2, animals
1000 underwent 4 training trials each (max. 90s), with varying starting positions. Once they climbed
1001 the platform, they were left to wait there for 10 s before being transferred back to the home
1002 cage. Animals that did not find the platform within 90 s were guided to the platform until they
1003 climbed it and left to wait on the platform for 10 s, before being transferred back to the home
1004 cage. On day 2, after the second training trial, and on day 3, a probe trial (60 s duration)
1005 without the platform was conducted. The time spent in the area where the platform was
1006 previously located, the time spent in the quadrant that previously contained the platform, the
1007 latency to the platform area, and the average minimum distance to the platform area were
1008 used to approximate successful spatial learning and memory. The total travel distance served
1009 as a measure for locomotor behavior, and the average distance to the wall were analyzed to
1010 compare thigmotactic behavior as well as searching strategies (i.e., circling around the pool).

1011 *Fiber photometry recordings.* Approximately 3 weeks after surgery, animals were
1012 habituated to the experimenter, set-up, and head fixation on a linear treadmill (200–100 500
1013 2100 and 700–100 100 0010; *Luigs & Neumann*). Fiber photometry recordings were
1014 performed using two *pyPhotometry* systems[100] (*Open Ephys*) controlling multicolor LED light
1015 sources (pE-4000; *CoolLED*) connected to the input ports of dichroic cubes (FMC5_E1(400–
1016 480)_F1(500–540)_E2(555-570)_F2(580–680)_S; *Doric Lenses*) as reported previously[13]. In
1017 brief, excitation light for quasi-isosbestic (405/10 nm) and calcium-dependent (470/10 nm)
1018 activation of jGCaMP8m was delivered in a temporally interleaved manner into the 400-480
1019 nm input port of the dichroic cube, while excitation light for jRGECO1a (555-570 nm) was
1020 delivered via the 555-570 nm port. We also included excitation at 405/10 nm as a control

channel when using jRGECO1a, as the indicator has been shown to be largely insensitive to calcium when excited at this wavelength[101], but we note that the efficiency of jRGECO1a excitation at 405 nm is very low (which, to a milder degree, is also true for jGCaMP8m). Hence, the recorded signal, which besides indicator fluorescence also contains autofluorescence originating from fiber optics and brain tissue[102], is likely composed differently and should not be over-interpreted. Emission light between 500-540 nm (jGCaMP8m) and 580-680 nm (jRGECO1a) was measured using photodetectors (DFD_FOA_FC; *Doric Lenses*), and digitized by the *pyPhotometry*-board at 130 Hz. Mice were connected to the dichroic cubes with low-autofluorescence patch cords (MFP_400/430/3000-0.57_1m_FC-ZF1.25(F)_LAF: 400 µm diameter, 0.57 NA; *Doric lenses*) via zirconia mating sleeves (SLEEVE_ZR_1.25; *Doric Lenses*). Simultaneously, the left eye of the mouse was monitored using a monochrome camera equipped with a macro-objective (DMK 22UX249 and TMN 1.0/50; *The Imaging Source*) and a 780 nm long-pass filter (FGL780; *Thorlabs*) under infrared illumination. Single video frames were triggered at 30 Hz with a voltage signal provided by an NI-DAQ-card (PCIe-6323; *National Instruments*), which was in addition fed to the *pyPhotometry* system for data synchronization.

Fiber photometry analysis. Single-sample outliers were removed from raw traces by applying a moving median filter with a window size of 3 sampling points, before traces of quasi-isosbestic and ligand-dependent fluorescence were detrended by fitting a double-exponential function to the respective trace and dividing the trace by the fitted curve, (accounting for bleaching components resulting both from the indicator and from the fiber optics[103]). Traces were then band-pass filtered (1/60-30 Hz; 3th order Butterworth filter) using *MATLAB*'s 'butter', and 'filtfilt' functions in order to remove signal components resulting from remaining bleaching and high frequency noise. The difference between the corrected functional and quasi-isosbestic traces was then taken as the functional signal, ΔF. Pupil edges (horizontal, vertical, and both diagonals) were extracted from each frame using *DeepLabCut*[104], and the pupil diameter was defined as the average distance of opposing edges in each frame. The pupil diameter was then smoothed with a window size of 250 ms (using the *MATLAB* functions 'resample' and 'smooth'). Animal position was recorded using the treadmill-software provided by *Luigs & Neumann*, smoothed by using a moving median filter with a window size of 500 ms, and speed was calculated as the derivative of animal position. For the experiments reported in this manuscript, the treadmill was largely immobilized to minimize locomotion-related pupil dilation. Yet, attempts of the animals to start locomotion could be detected, and trials in which treadmill movement exceeded 5 mm/s were excluded from further analysis. All data was re-sampled to 100 Hz for further processing. To detect periods of pupil dilation, peaks were detected in the derivative of pupil diameter using using *MATLAB*'s 'findpeaks' function, with a minimum peak prominence of the mean plus three standard deviation of the whole trace, and a minimum peak distance of 3 seconds. Photometry, pupil, and treadmill recordings were then then cropped and aligned in a time window starting 2 seconds before and ending 5 seconds after each peak.

1060 *Optogenetic manipulation of LC activity.* General procedures for optogenetic
1061 experiments were identical to fiber photometry experiments, except for the delivery of
1062 optogenetic stimuli. Stimuli were generated using custom-written *MATLAB* scripts actuating
1063 on an NI-DAQ-card (USB-6001; *National Instruments*), controlling a 633 nm diode laser (633-
1064 100; *Omicron Laserage*) housed in a laser combiner system (LightHUB; *Omicron Laserage*). The
1065 laser combiner was coupled to the optical fiber implants using a 1 × 2 step-index multimode
1066 fiber optic coupler (200 µm core diameter, 0.37 NA; SBP(2)_200/220/900-0.37_2m_FCM-
1067 2xZF1.25; *Doric Lenses*) via zirconia mating sleeves (SLEEVE_ZR_1.25; *Doric Lenses*) wrapped
1068 with black shrinking tubes to avoid light emission from the coupling interface. To activate
1069 ChrimsonR, pulse trains (633 nm, ~5 mW at each fiber end, 20 ms pulse duration, 20 Hz
1070 repetition rate) of 4 s duration were used. 30 stimuli were presented at an inter-stimulus-
1071 interval of 30 s. Pupil diameter was extracted from videographic images as for fiber
1072 photometry experiments, cropped, and aligned to optogenetic stimulation in a time window
1073 starting 5 seconds before and ending 20 seconds after each stimulus onset. Pupil diameter
1074 was then normalized to the median pupil diameter during the second before stimulus onset.

1075 *Statistics.* For histological data, one-way ANOVA was performed; when significant,
1076 post-hoc comparisons between groups were performed using Tukey's honestly significant
1077 difference criterion which controls for inflated risk of type-1 error (false positives) following
1078 multiple comparisons (using *MATLAB*'s 'anova1' and 'multcompare' functions). For behavioral
1079 data, two-way ANOVA was performed to identify differences between genotypes, sexes, and
1080 interactions thereof, using the software *Graphpad Prism*. All statistical tests were two-tailed,
1081 with a type-1 error risk set to $\alpha = 0.05$. In all figures, error bars correspond to standard error
1082 of the mean.

1083

1084 **Author contributions: CW**: Investigation, Validation, Data curation, Formal analysis, Writing –
1085 review & editing. **LSE**: Investigation, Validation, Data curation, Formal analysis, Visualization,
1086 Writing – review & editing. **MM**: Validation, Data curation, Formal analysis, Visualization,
1087 Software, Writing – review & editing, Funding acquisition. **KS**: Investigation, Validation,
1088 Writing – review & editing. **FM**: Validation, Methodology, Writing – review & editing,
1089 Supervision, Resources. **JSW**: Conceptualization, Methodology, Validation, Writing – review &
1090 editing, Supervision, Resources, Funding acquisition. **AD**: Conceptualization, Investigation,
1091 Validation, Data curation, Formal analysis, Visualization, Software, Writing – original draft,
1092 Writing – review & editing, Supervision.

1093

1094 **Acknowledgements:** The authors gratefully acknowledge Dr. Ingke Braren for production of
1095 viral constructs and Stefan Schillemeit for expert technical support with histology. We thank
1096 Prof. Dr. Bernardo Sabatini for the kindly gifting the rAAV2/9-EF1a-DO-DIO-tdTomato-eGFP
1097 construct (*AddGene* plasmid #37120), the GENIE Project for gifting pGP-AAV-syn-jGCaMP8m-

WPRE (*AddGene* plasmid #162375), Douglas Kim, *PhD*, and the GENIE Project for gifting pGP-CMV-NES-jRGECO1a (*AddGene* plasmid #61563), and Prof. Dr. Susumu Tonegawa for kindly providing the *Net*^{cre} line. We thank Patricia Jensen, *PhD*, and Nick Plummer, *PhD*, for helpful discussions on the different approaches of creating transgenic mouse lines. We thankfully acknowledge the support of the Core Facility Live Cell Imaging Mannheim (LIMa), and the data storage service SDS@hd supported by the Ministry of Science, Research and the Arts Baden-Württemberg (MWK) and the German Research Foundation (DFG) through grant INST 35/1503-1 FUGG. MM is supported by the *Alexander von Humboldt Stiftung*, and by the *Fondation Bettencourt-Schueller*. This work was supported by the German Research Foundation (DFG, grant agreement: 178316478-B8 to JSW).

Data Availability Statement: all primary data and code will be made available in the peer-reviewed version of the paper.

Conflict of interest: The authors declare no conflict of interest.

References

1. Sturrock, R. R. & Rao, K. A. A QUANTITATIVE HISTOLOGICAL STUDY OF NEURONAL LOSS FROM THE LOCUS COERULEUS OF AGEING MICE. *Neuropathol. Appl. Neurobiol.* **11**, 55–60 (1985).
2. Poe, G. R. *et al.* Locus coeruleus: a new look at the blue spot. *Nat. Rev. Neurosci.* **21**, 644–659 (2020).
3. Chandler, D. J. *et al.* Redefining Noradrenergic Neuromodulation of Behavior: Impacts of a Modular Locus Coeruleus Architecture. *J. Neurosci. Off. J. Soc. Neurosci.* **39**, 8239–8249 (2019).
4. Schwarz, L. A. & Luo, L. Organization of the locus coeruleus-norepinephrine system. *Curr. Biol. CB* **25**, R1051–R1056 (2015).
5. Szot, P. Common factors among Alzheimer's disease, Parkinson's disease, and epilepsy: possible role of the noradrenergic nervous system. *Epilepsia* **53 Suppl 1**, 61–66 (2012).
6. Morris, L. S., McCall, J. G., Charney, D. S. & Murrough, J. W. The role of the locus coeruleus in the generation of pathological anxiety. *Brain Neurosci. Adv.* **4**, 2398212820930321 (2020).
7. McBurney-Lin, J., Lu, J., Zuo, Y. & Yang, H. Locus coeruleus-norepinephrine modulation of sensory processing and perception: A focused review. *Neurosci. Biobehav. Rev.* **105**, 190–199 (2019).
8. Aston-Jones, G. & Waterhouse, B. Locus coeruleus: From global projection system to adaptive regulation of behavior. *Brain Res.* **1645**, 75–78 (2016).
9. Waterhouse, B. D. & Navarra, R. L. The locus coeruleus-norepinephrine system and sensory signal processing: A historical review and current perspectives. *Brain Res.* **1709**, 1–15 (2019).
10. Breton-Provencher, V., Drummond, G. T., Feng, J., Li, Y. & Sur, M. Spatiotemporal dynamics of noradrenaline during learned behaviour. *Nature* **606**, 732–738 (2022).
11. Su, Z. & Cohen, J. Y. Two types of locus coeruleus norepinephrine neurons drive reinforcement learning. Preprint at https://doi.org/10.1101/2022.12.08.519670 (2022).
12. Tanguay, E., Bouchard, S.-J., Lévesque, M., De Koninck, P. & Breton-Provencher, V. Shining light on the noradrenergic system. *Neurophotonics* **10**, (2023).
13. Kagiampaki, Z. *et al.* Sensitive multicolor indicators for monitoring norepinephrine in vivo. *Nat. Methods* (2023) doi:10.1038/s41592-023-01959-z.
14. Feng, J. *et al.* A Genetically Encoded Fluorescent Sensor for Rapid and Specific In Vivo Detection of Norepinephrine. *Neuron* **102**, 745-761.e8 (2019).
15. Sun, F. *et al.* A Genetically Encoded Fluorescent Sensor Enables Rapid and Specific Detection of Dopamine in Flies, Fish, and Mice. *Cell* **174**, 481-496.e19 (2018).
16. Patriarchi, T. *et al.* Ultrafast neuronal imaging of dopamine dynamics with designed genetically encoded sensors. *Science* **360**, eaat4422 (2018).

17. Patriarchi, T. *et al.* An expanded palette of dopamine sensors for multiplex imaging in vivo. *Nat. Methods* **17**, 1147–1155 (2020).
18. Gong, S. *et al.* Targeting Cre Recombinase to Specific Neuron Populations with Bacterial Artificial Chromosome Constructs. *J. Neurosci.* **27**, 9817–9823 (2007).
19. Tillage, R. P. *et al.* Elimination of galanin synthesis in noradrenergic neurons reduces galanin in select brain areas and promotes active coping behaviors. *Brain Struct. Funct.* **225**, 785–803 (2020).
20. Yu, J. *et al.* Cell-specific expression of Cre recombinase in rat noradrenergic neurons via CRISPR-Cas9 system. *Neuroscience* S0306452224003452 (2024) doi:10.1016/j.neuroscience.2024.07.032.
21. Wagatsuma, A. *et al.* Locus coeruleus input to hippocampal CA3 drives single-trial learning of a novel context. *Proc. Natl. Acad. Sci.* **115**, E310–E316 (2018).
22. Savitt, J. M., Jang, S. S., Mu, W., Dawson, V. L. & Dawson, T. M. Bcl-x is required for proper development of the mouse substantia nigra. *J. Neurosci. Off. J. Soc. Neurosci.* **25**, 6721–6728 (2005).
23. Lindeberg, J. *et al.* Transgenic expression of Cre recombinase from the tyrosine hydroxylase locus: Transgenic Expression of Cre Recombinase. *genesis* **40**, 67–73 (2004).
24. Witten, I. B. *et al.* Recombinase-Driver Rat Lines: Tools, Techniques, and Optogenetic Application to Dopamine-Mediated Reinforcement. *Neuron* **72**, 721–733 (2011).
25. Hwang, D. Y., Carlezon, W. A., Isacson, O. & Kim, K. S. A high-efficiency synthetic promoter that drives transgene expression selectively in noradrenergic neurons. *Hum. Gene Ther.* **12**, 1731–1740 (2001).
26. Bacon, T. J., Pickering, A. E. & Mellor, J. R. Noradrenaline Release from Locus Coeruleus Terminals in the Hippocampus Enhances Excitation-Spike Coupling in CA1 Pyramidal Neurons Via β-Adrenoceptors. *Cereb. Cortex* **30**, 6135–6151 (2020).
27. Li, Y. *et al.* Retrograde optogenetic characterization of the pontospinal module of the locus coeruleus with a canine adenoviral vector. *Brain Res.* **1641**, 274–290 (2016).
28. Hayat, H. *et al.* Locus coeruleus norepinephrine activity mediates sensory-evoked awakenings from sleep. *Sci. Adv.* **6**, eaaz4232 (2020).
29. Schmidt-Supprian, M. & Rajewsky, K. Vagaries of conditional gene targeting. *Nat. Immunol.* **8**, 665–668 (2007).
30. Harno, E., Cottrell, E. C. & White, A. Metabolic pitfalls of CNS Cre-based technology. *Cell Metab.* **18**, 21–28 (2013).
31. Matthaei, K. I. Genetically manipulated mice: a powerful tool with unsuspected caveats. *J. Physiol.* **582**, 481–488 (2007).
32. Maheu, M., Donner, T. H. & Wiegert, J. S. Serotonergic and noradrenergic interactions in pupil-linked arousal. Preprint at https://doi.org/10.1101/2025.03.26.644382 (2025).
33. Sohal, V. S., Zhang, F., Yizhar, O. & Deisseroth, K. Parvalbumin neurons and gamma rhythms enhance cortical circuit performance. *Nature* **459**, 698–702 (2009).
34. Hitoshi, N., Ken-ichi, Y. & Jun-ichi, M. Efficient selection for high-expression transfectants with a novel eukaryotic vector. *Gene* **108**, 193–199 (1991).
35. Stringer, C., Wang, T., Michaelos, M. & Pachitariu, M. Cellpose: a generalist algorithm for cellular segmentation. *Nat. Methods* **18**, 100–106 (2021).
36. Pachitariu, M. & Stringer, C. Cellpose 2.0: how to train your own model. *Nat. Methods* **19**, 1634–1641 (2022).
37. George Paxinos & Keith B.J. Franklin. *Paxinos and Franklin's the Mouse Brain in Stereotaxic Coordinates, Compact: The Coronal Plates and Diagrams*. (2019).
38. Fischer, K. B., Collins, H. K. & Callaway, E. M. Sources of off-target expression from recombinase-dependent AAV vectors and mitigation with cross-over insensitive ATG-out vectors. *Proc. Natl. Acad. Sci. U. S. A.* 201915974 (2019) doi:10.1073/pnas.1915974116.
39. Lammel, S. *et al.* Diversity of transgenic mouse models for selective targeting of midbrain dopamine neurons. *Neuron* **85**, 429–438 (2015).
40. Kügler, S. Tissue-Specific Promoters in the CNS. in *Gene Therapy for Neurological Disorders* (ed. Manfredsson, F. P.) vol. 1382 81–91 (Springer New York, New York, NY, 2016).
41. Thiel, G., Greengard, P. & Südhof, T. C. Characterization of tissue-specific transcription by the human synapsin I gene promoter. *Proc. Natl. Acad. Sci.* **88**, 3431–3435 (1991).
42. Watakabe, A. *et al.* Comparative analyses of adeno-associated viral vector serotypes 1, 2, 5, 8 and 9 in marmoset, mouse and macaque cerebral cortex. *Neurosci. Res.* **93**, 144–157 (2015).
43. Rorabaugh, J. M. *et al.* Chemogenetic locus coeruleus activation restores reversal learning in a rat model of Alzheimer's disease. *Brain* **140**, 3023–3038 (2017).

44. Stevens, L. *et al.* Optimized Parameters for Transducing the Locus Coeruleus Using Canine Adenovirus Type 2 (CAV2) Vector in Rats for Chemogenetic Modulation Research. *Front. Neurosci.* **15**, 663337 (2021).
45. Saunders, A., Johnson, C. A. & Sabatini, B. L. Novel recombinant adeno-associated viruses for Cre activated and inactivated transgene expression in neurons. *Front. Neural Circuits* **6**, (2012).
46. Chen, E. *et al.* Altered Baseline and Nicotine-Mediated Behavioral and Cholinergic Profiles in ChAT-Cre Mouse Lines. *J. Neurosci. Off. J. Soc. Neurosci.* **38**, 2177–2188 (2018).
47. Costa, K. M., Schenkel, D. & Roeper, J. Sex-dependent alterations in behavior, drug responses and dopamine transporter expression in heterozygous DAT-Cre mice. *Sci. Rep.* **11**, 3334 (2021).
48. Chohan, M. O., Esses, S., Haft, J., Ahmari, S. E. & Veenstra-VanderWeele, J. Altered baseline and amphetamine-mediated behavioral profiles in dopamine transporter Cre (DAT-Ires-Cre) mice compared to tyrosine hydroxylase Cre (TH-Cre) mice. *Psychopharmacology (Berl.)* **237**, 3553–3568 (2020).
49. Ross, J. A. & Van Bockstaele, E. J. The Locus Coeruleus- Norepinephrine System in Stress and Arousal: Unraveling Historical, Current, and Future Perspectives. *Front. Psychiatry* **11**, 601519 (2021).
50. Belzung, C. Chapter 4.11 Measuring rodent exploratory behavior. in *Techniques in the Behavioral and Neural Sciences* vol. 13 738–749 (Elsevier, 1999).
51. Pellow, S., Chopin, P., File, S. E. & Briley, M. Validation of open : closed arm entries in an elevated plus-maze as a measure of anxiety in the rat. *J. Neurosci. Methods* **14**, 149–167 (1985).
52. Takeuchi, T. *et al.* Locus coeruleus and dopaminergic consolidation of everyday memory. *Nature* **537**, 357–362 (2016).
53. Kempadoo, K. A., Mosharov, E. V., Choi, S. J., Sulzer, D. & Kandel, E. R. Dopamine release from the locus coeruleus to the dorsal hippocampus promotes spatial learning and memory. *Proc. Natl. Acad. Sci.* **113**, 14835–14840 (2016).
54. Lalonde, R. The neurobiological basis of spontaneous alternation. *Neurosci. Biobehav. Rev.* **26**, 91–104 (2002).
55. Steinberg, H., Rushton, R. & Tinson, C. Modification of the Effects of an Amphetamine–Barbiturate Mixture by the Past Experience of Rats. *Nature* **192**, 533–535 (1961).
56. Morris, R. G. M. Spatial localization does not require the presence of local cues. *Learn. Motiv.* **12**, 239–260 (1981).
57. Kabanova, A., Cavani, E., Logothetis, N. K. & Eschenko, O. Feasibility of Canine Adenovirus Type 2 (CAV2) Based Vector for the Locus Coeruleus Optogenetic Activation in Non-Transgenic Rats: Implications for Functional Studies. *Brain Sci.* **12**, 904 (2022).
58. Vazey, E. M. & Aston-Jones, G. Designer receptor manipulations reveal a role of the locus coeruleus noradrenergic system in isoflurane general anesthesia. *Proc. Natl. Acad. Sci.* **111**, 3859–3864 (2014).
59. Zhang, Y. *et al.* Fast and sensitive GCaMP calcium indicators for imaging neural populations. *Nature* (2023) doi:10.1038/s41586-023-05828-9.
60. Dana, H. *et al.* Sensitive red protein calcium indicators for imaging neural activity. *eLife* **5**, e12727 (2016).
61. Breton-Provencher, V. & Sur, M. Active control of arousal by a locus coeruleus GABAergic circuit. *Nat. Neurosci.* **22**, 218–228 (2019).
62. Reimer, J. *et al.* Pupil fluctuations track rapid changes in adrenergic and cholinergic activity in cortex. *Nat. Commun.* **7**, 13289 (2016).
63. Klapoetke, N. C. *et al.* Independent optical excitation of distinct neural populations. *Nat. Methods* **11**, 338–346 (2014).
64. Shaner, N. C. *et al.* Improved monomeric red, orange and yellow fluorescent proteins derived from Discosoma sp. red fluorescent protein. *Nat. Biotechnol.* **22**, 1567–1572 (2004).
65. Vincent, S. R. Distributions of tyrosine hydroxylase-, dopamine-beta-hydroxylase-, and phenylethanolamine-N-methyltransferase-immunoreactive neurons in the brain of the hamster (Mesocricetus auratus). *J. Comp. Neurol.* **268**, 584–599 (1988).
66. Qin, H., Lu, J., Jin, W., Chen, X. & Fu, L. Multichannel fiber photometry for mapping axonal terminal activity in a restricted brain region in freely moving mice. *Neurophotonics* **6**, 1 (2019).
67. Pisanello, M. *et al.* The Three-Dimensional Signal Collection Field for Fiber Photometry in Brain Tissue. *Front. Neurosci.* **13**, 82 (2019).
68. Koga, K. *et al.* Ascending noradrenergic excitation from the locus coeruleus to the anterior cingulate cortex. *Mol. Brain* **13**, 49 (2020).
69. Nomura, S. *et al.* Combined Optogenetic Approaches Reveal Quantitative Dynamics of Endogenous Noradrenergic Transmission in the Brain. *iScience* **23**, 101710 (2020).

70. Nomura, S. *et al.* Noradrenalin and dopamine receptors both control cAMP-PKA signaling throughout the cerebral cortex. *Front. Cell. Neurosci.* **8**, 247 (2014).
71. Lavoie, A. & Liu, B. Canine Adenovirus 2: A Natural Choice for Brain Circuit Dissection. *Front. Mol. Neurosci.* **13**, 9 (2020).
72. Stevens, L. *et al.* A Feasibility Study to Investigate Chemogenetic Modulation of the Locus Coeruleus by Means of Single Unit Activity. *Front. Neurosci.* **14**, 162 (2020).
73. Antila, H. *et al.* A noradrenergic-hypothalamic neural substrate for stress-induced sleep disturbances. *Proc. Natl. Acad. Sci.* **119**, e2123528119 (2022).
74. Min, N., Joh, T. H., Kim, K. S., Peng, C. & Son, J. H. 5' Upstream DNA sequence of the rat tyrosine hydroxylase gene directs high-level and tissue-specific expression to catecholaminergic neurons in the central nervous system of transgenic mice. *Mol. Brain Res.* **27**, 281–289 (1994).
75. Rukhadze, I. *et al.* Catecholaminergic A1/C1 neurons contribute to the maintenance of upper airway muscle tone but may not participate in NREM sleep-related depression of these muscles. *Respir. Physiol. Neurobiol.* **244**, 41–50 (2017).
76. Vuong, H. E., Pérez de Sevilla Müller, L., Hardi, C. N., McMahon, D. G. & Brecha, N. C. Heterogeneous transgene expression in the retinas of the TH-RFP, TH-Cre, TH-BAC-Cre and DAT-Cre mouse lines. *Neuroscience* **307**, 319–337 (2015).
77. Gábriel, R., Erdélyi, F., Szabó, G., Lawrence, J. J. & Wilhelm, M. Ectopic transgene expression in the retina of four transgenic mouse lines. *Brain Struct. Funct.* **221**, 3729–3741 (2016).
78. Cardozo Pinto, D. F. *et al.* Characterization of transgenic mouse models targeting neuromodulatory systems reveals organizational principles of the dorsal raphe. *Nat. Commun.* **10**, 4633 (2019).
79. Papathanou, M., Dumas, S., Pettersson, H., Olson, L. & Wallén-Mackenzie, Å. Off-Target Effects in Transgenic Mice: Characterization of Dopamine Transporter (DAT)-Cre Transgenic Mouse Lines Exposes Multiple Non-Dopaminergic Neuronal Clusters Available for Selective Targeting within Limbic Neurocircuitry. *eNeuro* **6**, (2019).
80. Hu, H., Cavendish, J. Z. & Agmon, A. Not all that glitters is gold: off-target recombination in the somatostatin-IRES-Cre mouse line labels a subset of fast-spiking interneurons. *Front. Neural Circuits* **7**, 195 (2013).
81. Zhang, B. *et al.* The specificity and role of microglia in epileptogenesis in mouse models of tuberous sclerosis complex. *Epilepsia* **59**, 1796–1806 (2018).
82. Stuber, G. D., Stamatakis, A. M. & Kantak, P. A. Considerations when using cre-driver rodent lines for studying ventral tegmental area circuitry. *Neuron* **85**, 439–445 (2015).
83. Song, A. J. & Palmiter, R. D. Detecting and Avoiding Problems When Using the Cre-lox System. *Trends Genet. TIG* **34**, 333–340 (2018).
84. Prabhakar, A., Vujovic, D., Cui, L., Olson, W. & Luo, W. Leaky expression of channelrhodopsin-2 (ChR2) in Ai32 mouse lines. *PLOS ONE* **14**, e0213326 (2019).
85. Mariscal, P. *et al.* Sexual differences in locus coeruleus neurons and related behavior in C57BL/6J mice. *Biol. Sex Differ.* **14**, 64 (2023).
86. An, X.-L. *et al.* Strain and Sex Differences in Anxiety-Like and Social Behaviors in C57BL/6J and BALB/cJ Mice. *Exp. Anim.* **60**, 111–123 (2011).
87. Fritz, A., Amrein, I. & Wolfer, D. P. Similar reliability and equivalent performance of female and male mice in the open field and water-maze place navigation task. *Am. J. Med. Genet. C Semin. Med. Genet.* **175**, 380–391 (2017).
88. Thanky, N. R., Son, J. H. & Herbison, A. E. Sex differences in the regulation of tyrosine hydroxylase gene transcription by estrogen in the locus coeruleus of TH9-LacZ transgenic mice. *Mol. Brain Res.* **104**, 220–226 (2002).
89. Sorge, R. E. *et al.* Olfactory exposure to males, including men, causes stress and related analgesia in rodents. *Nat. Methods* **11**, 629–632 (2014).
90. Georgiou, P. *et al.* Experimenters' sex modulates mouse behaviors and neural responses to ketamine via corticotropin releasing factor. *Nat. Neurosci.* **25**, 1191–1200 (2022).
91. Gouveia, K. & Hurst, J. L. Optimising reliability of mouse performance in behavioural testing: the major role of non-aversive handling. *Sci. Rep.* **7**, 44999 (2017).
92. Ueno, H. *et al.* Effects of repetitive gentle handling of male C57BL/6NCrl mice on comparative behavioural test results. *Sci. Rep.* **10**, 3509 (2020).
93. Mandillo, S. *et al.* Reliability, robustness, and reproducibility in mouse behavioral phenotyping: a cross-laboratory study. *Physiol. Genomics* **34**, 243–255 (2008).

94. Crabbe, J. C., Wahlsten, D. & Dudek, B. C. Genetics of Mouse Behavior: Interactions with Laboratory Environment. *Science* **284**, 1670–1672 (1999).
95. Lui, S., Brink, A. K. & Corbit, L. H. Optogenetic stimulation of the locus coeruleus enhances appetitive extinction in rats. *eLife* **12**, RP89267 (2024).
96. Botterill, J. J. *et al.* Off-Target Expression of Cre-Dependent Adeno-Associated Viruses in Wild-Type C57BL/6J Mice. *eneuro* **8**, ENEURO.0363-21.2021 (2021).
97. Haery, L. *et al.* Adeno-Associated Virus Technologies and Methods for Targeted Neuronal Manipulation. *Front. Neuroanat.* **13**, 93 (2019).
98. Cormack, B. P., Valdivia, R. H. & Falkow, S. FACS-optimized mutants of the green fluorescent protein (GFP). *Gene* **173**, 33–38 (1996).
99. Schindelin, J. *et al.* Fiji: an open-source platform for biological-image analysis. *Nat. Methods* **9**, 676–682 (2012).
100. Akam, T. & Walton, M. E. pyPhotometry: Open source Python based hardware and software for fiber photometry data acquisition. *Sci. Rep.* **9**, 3521 (2019).
101. Molina, R. S. *et al.* Understanding the Fluorescence Change in Red Genetically Encoded Calcium Ion Indicators. *Biophys. J.* **116**, 1873–1886 (2019).
102. Formozov, A., Dieter, A. & Wiegert, J. S. A flexible and versatile system for multi-color fiber photometry and optogenetic manipulation. *Cell Rep. Methods* 100418 (2023) doi:10.1016/j.crmeth.2023.100418.
103. Simpson, E. H. *et al.* Lights, fiber, action! A primer on in vivo fiber photometry. *Neuron* **112**, 718–739 (2024).
104. Mathis, A. *et al.* DeepLabCut: markerless pose estimation of user-defined body parts with deep learning. *Nat. Neurosci.* **21**, 1281–1289 (2018).

– Supplementary Material 3 –

Supplementary table 1:	Cre driver lines to target the NE system in mice
Supplementary table 1:	Statistical analysis of behavioral screening
Supplementary Figure S1:	Additional examples of eGFP expression in *Th*^{cre} mice
Supplementary Figure S2:	Decoupling of TH and eGFP expression in *Th*^{cre} mice
Supplementary Figure S3:	Independence of histology quantification on the overlap threshold of cell masks
Supplementary Figure S4:	Leakage of cre-dependent virus in wild-type mice
Supplementary Figure S5:	Agreement between *CellPose*-based and human-based cell segmentation
Supplementary Figure S6:	Specificity of cre-dependent transgene expression in the VTA of *Th*^{cre} mice
Supplementary Figure S7:	Comparison of native *eGFP* expression with anti-*GFP* staining
Supplementary Figure S8:	Ectopic transgene expression across model systems
Supplementary Figure S9:	Effects of serotype and injection volume on viral spread
Supplementary Figure S10:	Supplementary readouts obtained in the open field test
Supplementary Figure S11:	Supplementary readouts obtained in the elevated plus maze
Supplementary Figure S12:	Supplementary readouts obtained in the Y-maze
Supplementary Figure S13:	Morris water maze during training sessions
Supplementary Figure S14:	Supplementary readouts obtained in the Morris water maze

Supplementary table 1 | Cre driver lines to target the NE system in mice. Bold font indicates mouse lines used in this study. Grey font indicates mouse lines which are not readily available from any vendor.

strain name	*trivial name*	*gene*	*strategy*	*provider*	*strain ID*	*reference*
B6.Cg-Dbh$^{tm3.2(cre)Pjen}$/J	***Dbh^{cre}***	Dopamine-β-Hydroxylase	knock-in/ knock-out	*Jackson Laboratory*	033951	Tillage et al.[19]
Tg(Dbh-cre)KH210Gsat/Mmucd	*Dbh^{cre}*	Dopamine-β-Hydroxylase	BAC	*Mutant Mouse Resource & Research Centers*	036734-UCD	Gong et al.[18]
Tg(Dbh-cre)KH212Gsat/Mmucd	*Dbh^{cre}*	Dopamine-β-Hydroxylase	BAC	*Mutant Mouse Resource & Research Centers*	032081-UCD	Gong et al.[18]
B6.Cg-7630403G23 RikTg$^{(Th\text{-}cre)1Tmd}$/J	***Th^{cre}***	Tyrosine Hydroxylase	random insertion	*Jackson Laboratory*	008601	Savitt et al.[22]
B6.FVB(Cg)Tg(Th-cre)Fl172Gsat/Mmucd	*Th^{cre}*	Tyrosine Hydroxylase	BAC	*Mutant Mouse Resource & Research Centers*	031029-UCD	Gong et al.[18]
B6.129X1-Th$^{tm1(cre)Te}$/Kieg	*Th^{cre}*	Tyrosine Hydroxylase	Targeted mutation	*European Mouse Mutant Archive*	EM: 00254	Lindeberg et al.[23]
Tg(Slc6a2-cre)#Stl	***Net^{cre}***	Norepi-nephrine Transporter	BAC	–	–	Wagatsuma et al.[21]

Supplementary table 2 | Statistical analysis of behavioral screening. The table indicates results of a two-way ANOVA analyzing effects of genotype (GT), sex, or interactions thereof (×) in the mouse lines included in this study on different aspects of behavior in the in the open field test (OF), elevated plus maze (EPM), Y-maze (YM), and Morris water maze (MWM). All groups included 8 male and 8 female mice of each genotype. *p*-values below 0.05 are indicated in bold font. Note that multiple comparisons were not corrected in this table.

paradigm		***Dbh^{cre}***			***Net^{cre}***			***Th^{cre}***		
test	**readout**	**GT**	**Sex**	**×**	**GT**	**Sex**	**×**	**GT**	**Sex**	**×**
OF	*t* in center	$F = 0.45$ $p = 0.51$	$F = 0.39$ $p = 0.22$	$F = 1.60$ $p = 0.22$	$F = 0.54$ $p = 0.47$	$F = 3.93$ $p = 0.06$	$F = 0.01$ $p = 0.94$	$F = 0.01$ $p = 0.91$	$F = 4.22$ $p = 0.05$	$F = 4.37$ $p = 0.05$
	center crossings	$F = 0.01$ $p = 0.91$	$F = 0.41$ $p = 0.54$	$F = 1.87$ $p = 0.28$	$F = 0.02$ $p = 0.89$	$F = 0.14$ $p = 0.71$	$F = 0.05$ $p = 0.82$	$F = 0.01$ $p = 0.91$	$F = 1.34$ $p = 0.26$	$F = 0.33$ $p = 0.57$
	latency to center	$F = 1.33$ $p = 0.26$	$F = 1.00$ $p = 0.33$	$F = 0.11$ $p = 0.74$	$F = 1.27$ $p = 0.27$	$F = 0.29$ $p = 0.60$	$F = 1.00$ $p = 0.33$	$F = 1.10$ $p = 0.34$	$F = 2.96$ $p = 0.10$	$F = 2.89$ $p = 0.10$
	distance to wall	$F = 0.61$ $p = 0.44$	$F = 6.91$ $\mathbf{p = 0.01}$	$F = 3.26$ $p = 0.08$	$F = 0.73$ $p = 0.4$	$F = 2.31$ $p = 0.54$	$F = 0.39$ $p = 0.14$	$F = 3.34$ $p = 0.08$	$F = 2.09$ $p = 0.16$	$F = 6.41$ $\mathbf{p = 0.02}$
	t in border	$F = 1.52$ $p = 0.23$	$F = 11.7$ $\mathbf{p < 0.01}$	$F = 1.44$ $p = 0.24$	$F = 2.81$ $p = 0.11$	$F = 1.82$ $p = 0.19$	$F = 0.07$ $p = 0.79$	$F = 1.74$ $p = 0.20$	$F = 0.37$ $p = 0.55$	$F = 3.72$ $p = 0.06$
	travel distance	$F = 0.03$ $p = 0.87$	$F = 0.28$ $p = 0.60$	$F = 0.03$ $p = 0.87$	$F = 0.54$ $p = 0.47$	$F = 3.93$ $p = 0.06$	$F < 0.01$ $p = 0.94$	$F = 0.01$ $p = 0.94$	$F = 16.4$ $\mathbf{p < 0.01}$	$F < 0.01$ $p = 0.97$
	t in open arm	$F = 1.96$ $p = 0.17$	$F = 1.95$ $p = 0.17$	$F = 0.01$ $p = 0.91$	$F < 0.01$ $p = 0.93$	$F = 0.76$ $p = 0.39$	$F = 2.34$ $p = 0.14$	$F = 0.32$ $p = 0.57$	$F = 0.07$ $p = 0.79$	$F = 0.12$ $p = 0.73$
	open arm entries	$F = 1.91$ $p = 0.22$	$F = 0.01$ $p = 0.91$	$F = 0.17$ $p = 0.68$	$F = 0.75$ $p = 0.60$	$F = 0.07$ $p = 0.80$	$F = 0.21$ $p = 0.65$	$F = 0.14$ $p = 0.71$	$F = 0.03$ $p = 0.87$	$F = 0.33$ $p = 0.57$

EPM	open arm edges	$F < 0.01$ $p = 0.94$	$F = 5.52$ $\mathbf{p = 0.03}$	$F = 0.30$ $p = 0.59$	$F < 0.01$ $p = 0.95$	$F = 3.57$ $p = 0.07$	$F = 0.16$ $p = 0.69$	$F < 0.01$ $p = 0.95$	$F = 3.57$ $p = 0.07$	$F = 0.16$ $p = 0.69$
	t to leave center	$F = 0.01$ $p = 0.91$	$F = 5.02$ $p = 0.03$	$F < 0.01$ $p = 0.98$	$F = 2.59$ $p = 0.12$	$F = 2.12$ $p = 0.16$	$F < 0.01$ $p = 0.94$	$F = 4.19$ $p = 0.05$	$F = 0.61$ $p = 0.44$	$F = 0.12$ $p = 0.73$
	Rearing events	$F = 2.13$ $p = 0.16$	$F = 1.45$ $p = 0.16$	$F = 2.13$ $p = 0.16$	$F = 0.81$ $p = 0.38$	$F = 3.20$ $p = 0.08$	$F < 0.01$ $p = 0.93$	$F = 0.91$ $p = 0.35$	$F = 2.43$ $p = 0.13$	$F = 0.12$ $p = 0.73$
	t to rearing	$F = 2.11$ $p = 0.16$	$F = 1.41$ $p = 0.24$	$F = 0.04$ $p = 0.85$	$F = 2.28$ $p = 0.15$	$F = 2.77$ $p = 0.11$	$F = 0.95$ $p = 0.34$	$F = 0.26$ $p = 0.61$	$F = 0.26$ $p = 0.61$	$F = 4.43$ $\mathbf{p = 0.04}$
	t grooming	$F = 1.01$ $p = 0.32$	$F = 0.87$ $p = 0.36$	$F = 0.05$ $p = 0.82$	$F = 1.23$ $p = 0.26$	$F = 0.82$ $p = 0.37$	$F = 1.98$ $p = 0.17$	$F = 0.25$ $p = 0.62$	$F = 0.23$ $p = 0.63$	$F = 1.42$ $p = 0.24$
YM	alter-nations	$F = 1.30$ $p = 0.26$	$F = 1.62$ $p = 0.21$	$F = 0.24$ $p = 0.62$	$F = 2.48$ $p = 0.13$	$F = 2.32$ $p = 0.14$	$F = 0.02$ $p = 0.89$	$F = 0.23$ $p = 0.64$	$F = 2.95$ $p = 0.09$	$F = 0.31$ $p = 0.58$
	t/ transitions	$F = 0.04$ $p = 0.84$	$F = 0.76$ $p = 0.39$	$F = 2.55$ $p = 0.12$	$F = 3.04$ $p = 0.09$	$F = 2.95$ $p = 0.09$	$F = 0.31$ $p = 0.56$	$F = 3.04$ $p = 0.09$	$F = 0.20$ $p = 0.66$	$F = 11.2$ $\mathbf{p < 0.01}$
MWM day 2	*t* in platform	$F = 0.40$ $p = 0.54$	$F = 0.16$ $p = 0.69$	$F = 0.66$ $p = 0.42$	$F = 0.70$ $p = 0.41$	$F = 0.07$ $p = 0.79$	$F = 1.3$ $p = 0.26$	$F = 0.03$ $p = 0.87$	$F = 0.93$ $p = 0.34$	$F < 0.01$ $p = 0.93$
	t in quadrant	$F = 0.48$ $p = 0.49$	$F < 0.01$ $p = 0.99$	$F = 0.07$ $p = 0.79$	$F = 0.23$ $p = 0.64$	$F = 3.01$ $p = 0.09$	$F = 0.31$ $p = 0.58$	$F < 0.01$ $p = 0.95$	$F = 0.32$ $p = 0.57$	$F < 0.01$ $p = 0.94$
	t to platform	$F = 0.90$ $p = 0.35$	$F = 0.06$ $p = 0.81$	$F = 0.08$ $p = 0.78$	$F = 0.03$ $p = 0.86$	$F = 0.32$ $p = 0.58$	$F = 0.60$ $p = 0.44$	$F = 0.07$ $p = 0.79$	$F = 4.25$ $p = 0.05$	$F = 1.53$ $p = 0.23$
	distance to platform	$F = 0.23$ $p = 0.63$	$F = 1.63$ $p = 0.21$	$F = 2.40$ $p = 0.13$	$F = 0.26$ $p = 0.62$	$F = 2.96$ $p = 0.10$	$F < 0.01$ $p = 0.95$	$F = 0.05$ $p = 0.82$	$F = 1.30$ $p = 0.26$	$F = 0.27$ $p = 0.61$
	travel distance	$F = 0.04$ $p = 0.53$	$F = 0.29$ $p = 0.60$	$F = 0.58$ $p = 0.45$	$F = 0.88$ $p = 0.36$	$F = 2.48$ $p = 0.13$	$F = 0.02$ $p = 0.88$	$F = 0.04$ $p = 0.84$	$F < 0.01$ $p = 0.99$	$F = 0.46$ $p = 0.51$
	distance to wall	$F = 1.57$ $p = 0.24$	$F = 1.47$ $p = 0.24$	$F = 1.00$ $p = 0.32$	$F = 0.03$ $p = 0.87$	$F < 0.01$ $p = 0.99$	$F = 0.92$ $p = 0.35$	$F = 0.86$ $p = 0.36$	$F = 1.42$ $p = 0.24$	$F = 0.23$ $p = 0.63$
MWM day 3	*t* in platform	$F = 1.14$ $p = 0.29$	$F = 0.80$ $p = 0.38$	$F < 0.01$ $p = 0.94$	$F = 0.56$ $p = 0.46$	$F = 0.43$ $p = 0.52$	$F = 0.30$ $p = 0.59$	$F = 0.34$ $p = 0.56$	$F = 0.30$ $p = 0.59$	$F = 0.33$ $p = 0.57$
	t in quadrant	$F = 0.04$ $p = 0.85$	$F = 1.50$ $p = 0.23$	$F = 0.41$ $p = 0.52$	$F = 0.68$ $p = 0.42$	$F = 0.45$ $p = 0.51$	$F = 0.25$ $p = 0.62$	$F = 0.59$ $p = 0.45$	$F = 0.25$ $p = 0.62$	$F = 0.16$ $p = 0.69$
	t to platform	$F = 0.07$ $p = 0.80$	$F = 0.29$ $p = 0.60$	$F = 0.11$ $p = 0.75$	$F = 0.14$ $p = 0.71$	$F = 1.59$ $p = 0.22$	$F = 0.40$ $p = 0.53$	$F < 0.01$ $p = 0.97$	$F = 0.24$ $p = 0.63$	$F = 0.40$ $p = 0.53$
	distance to platform	$F = 0.11$ $p = 0.75$	$F = 0.49$ $p = 0.49$	$F = 0.01$ $p = 0.91$	$F = 0.88$ $p = 0.36$	$F = 0.09$ $p = 0.76$	$F = 2.84$ $p = 0.10$	$F = 0.07$ $p = 0.80$	$F = 4.0$ $p = 0.06$	$F = 0.04$ $p = 0.83$
	travel distance	$F = 0.06$ $p = 0.82$	$F = 0.28$ $p = 0.60$	$F = 0.55$ $p = 0.47$	$F = 1.24$ $p = 0.27$	$F = 0.79$ $p = 0.38$	$F = 0.05$ $p = 0.82$	$F = 0.13$ $p = 0.73$	$F = 0.05$ $p = 0.82$	$F < 0.01$ $p = 0.93$
	distance to wall	$F = 2.94$ $p = 0.10$	$F = 0.17$ $p = 0.69$	$F = 0.89$ $p = 0.35$	$F = 0.07$ $p = 0.79$	$F = 2.28$ $p = 0.14$	$F = 0.11$ $p = 0.75$	$F < 0.01$ $p = 0.93$	$F = 2.87$ $p = 0.10$	$F = 0.48$ $p = 0.50$

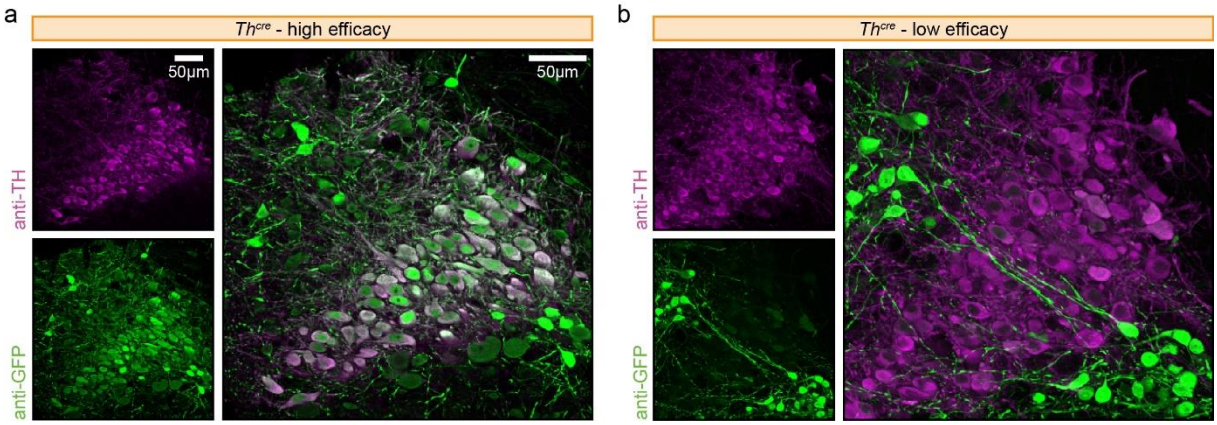

Figure S1 | Additional examples of eGFP expression in *Th^{cre}* mice. TH-expression (magenta) and eGFP expression (green) in exemplary *Th^{cre}* mice with high (**a**) and low efficacy (b). Scale bar: 50 µm.

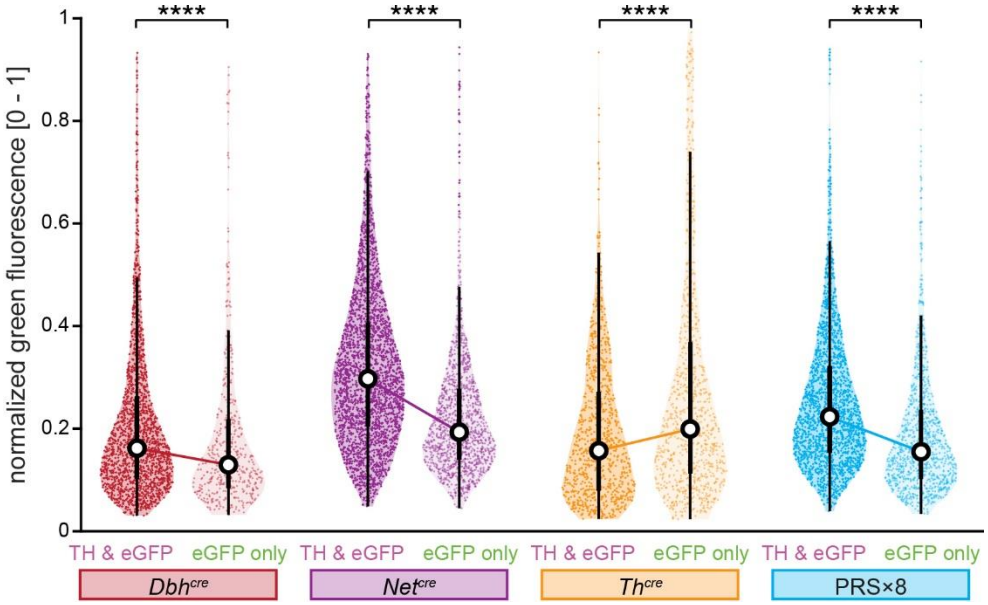

Figure S2 | Decoupling of TH and eGFP expression in the LC region of *Th^{cre}* mice. Normalized fluorescence in the green channel of neurons co-expressing TH and eGFP (i.e., true positives; left) and neurons expressing eGFP only (i.e., false positives; right) in *Dbh^{cre}* (red), *Net^{cre}* (magenta), *Th^{cre}* (orange) and PRS×8 mice (blue). Violin plots indicate 0th, 25th, 50th, 75th and 100th percentile, respectively. While normalized fluorescence of false positive neurons was lower as compared to true positive neurons in *Dbh^{cre}*, *Net^{cre}* and PRSx8 mice, normalized fluorescence of false positive neurons exceeded true positive neurons in *Th^{cre}* mice. ****: $p < 0.0001$ (Bonferroni-corrected Wilcoxon rank sum test). Numerical data underlying this figure can be found in supplementary material 1 (S1_Data.xlsx).

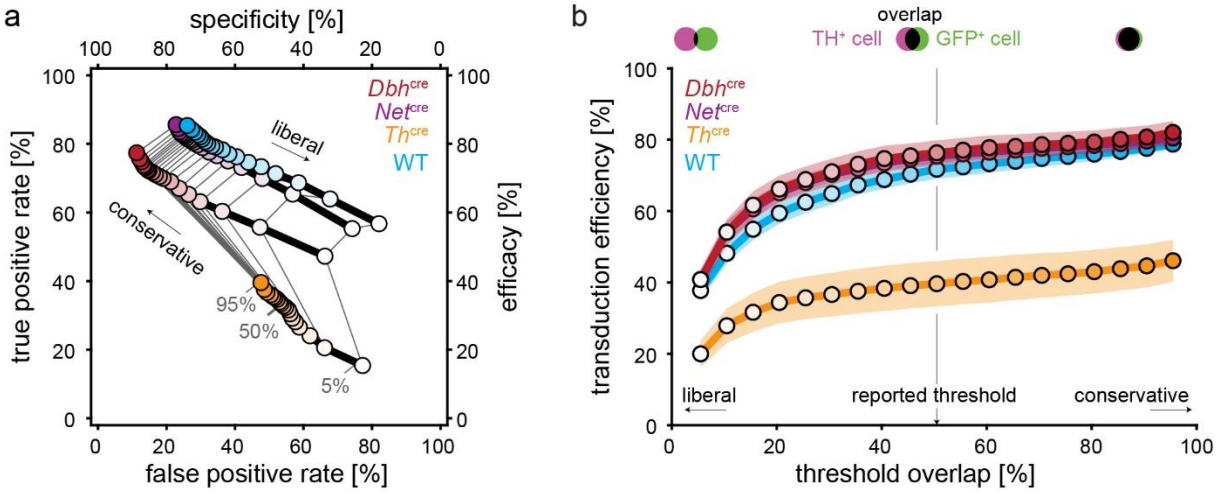

Figure S3 | Independence of histology quantification on the overlap threshold of cell masks. a, Efficacy and specificity from the 4 different model systems (as in Figure 1d) as a function of the threshold overlap parameter (light to dark colors; ranging from 5% to 95%, in steps of 5%) which defines the minimal overlap between *GFP*⁺ and *TH*⁺ channels for a *TH*⁺ cell to be also labeled as *GFP*⁺. **b**, Transduction efficiency (summarizing sensitivity and specificity in a single metric) from the 4 different model systems (as in Figure 1e) quantitatively varied as a function of the threshold overlap parameter. Importantly, conclusions were robust to this parameter choice as shown by the non-crossing of the curves. In the main text, we report values for a neutral threshold overlap parameter of 50%. Shading areas denote the standard error of the mean (n = 7).

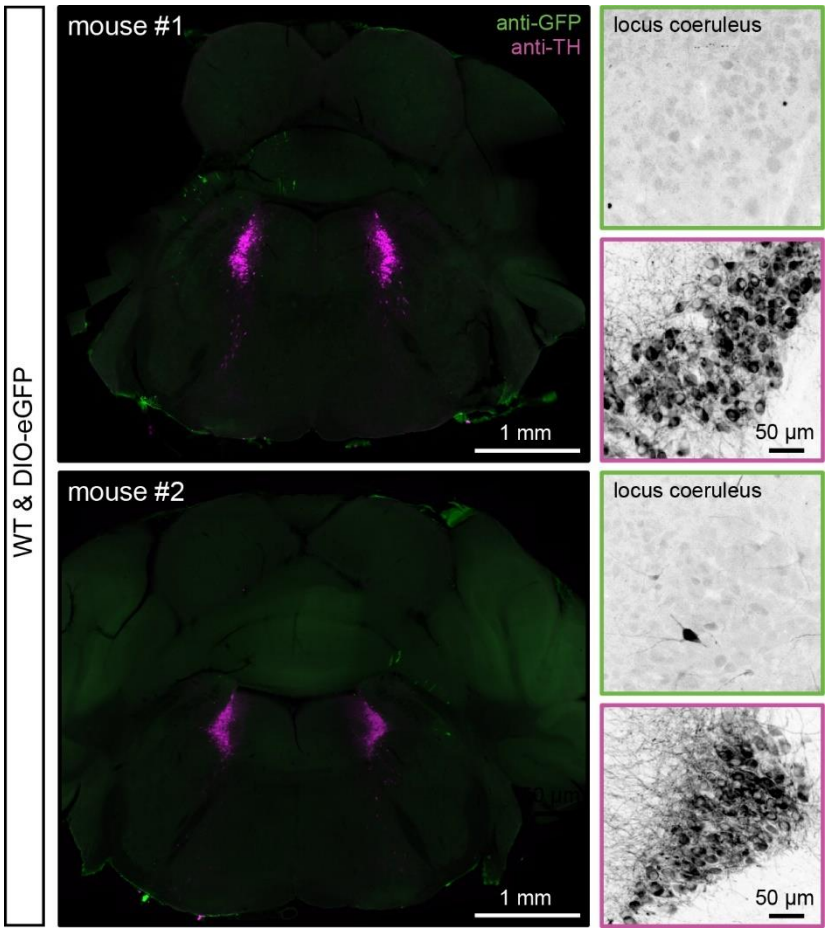

Figure S4 | Leakage of cre-dependent virus in wild-type mice. Immunohistochemical staining against *GFP* (green) and *TH* (magenta) in two wild-type mice injected with rAAV2/9-DIO-eGFP. *eGFP* expression was only observed in very few cells both within and outside of the LC.

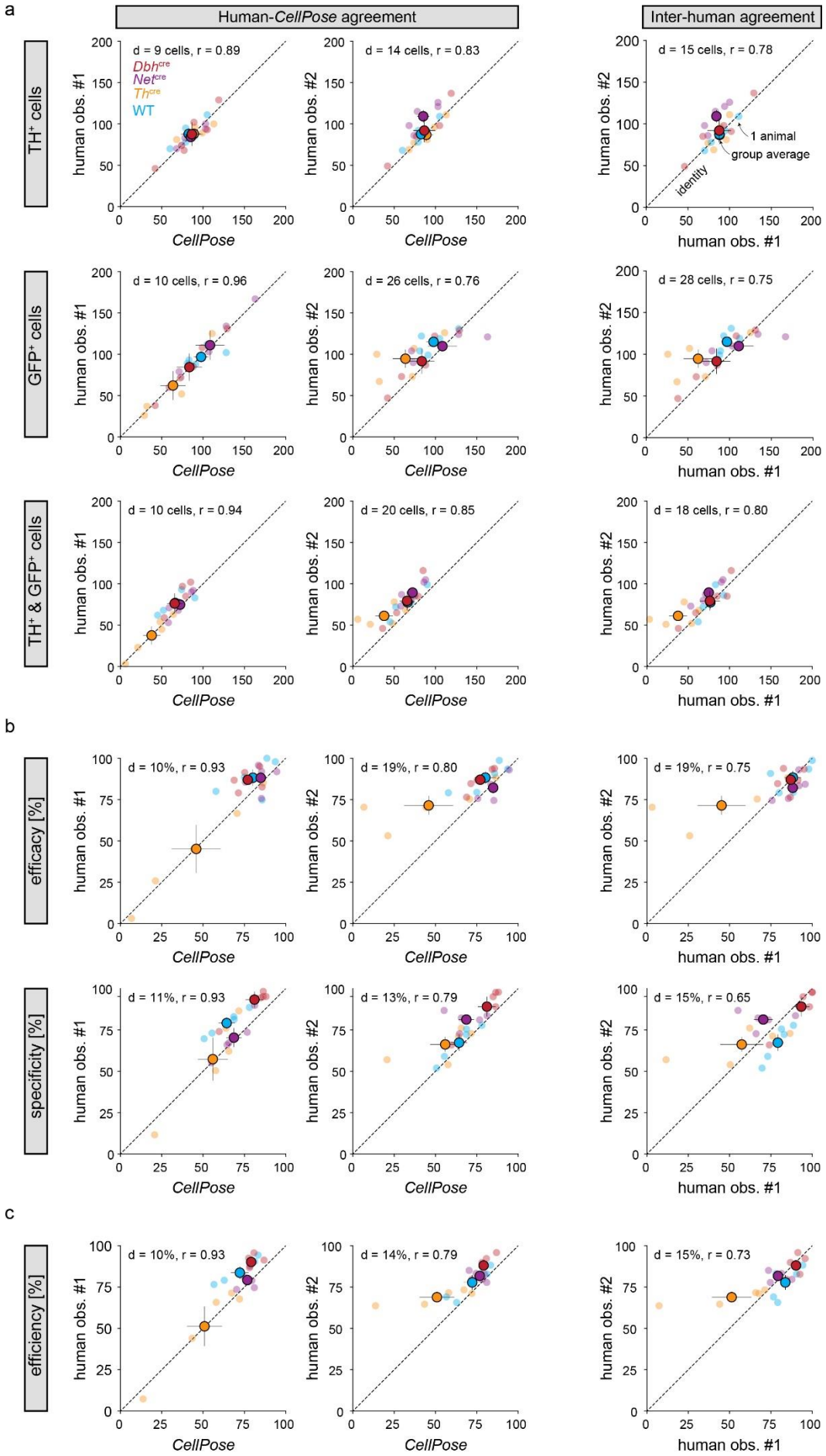
a
Human-CellPose agreement
Inter-human agreement
TH+ cells
GFP+ cells
TH+ & GFP+ cells
d = 9 cells, r = 0.89
Dbhcre
Netcre
Thcre
WT
d = 14 cells, r = 0.83
d = 15 cells, r = 0.78
1 animal
group average
identity
d = 10 cells, r = 0.96
d = 26 cells, r = 0.76
d = 28 cells, r = 0.75
d = 10 cells, r = 0.94
d = 20 cells, r = 0.85
d = 18 cells, r = 0.80
human obs. #1
human obs. #2
CellPose
b
efficacy [%]
specificity [%]
d = 10%, r = 0.93
d = 19%, r = 0.80
d = 19%, r = 0.75
d = 11%, r = 0.93
d = 13%, r = 0.79
d = 15%, r = 0.65
c
efficiency [%]
d = 10%, r = 0.93
d = 14%, r = 0.79
d = 15%, r = 0.73

1398

Figure S5 | Agreement between *CellPose*-based and human-based cell segmentation. a, Correlation of cell counts; **b**, Efficacy & specificity; **c**, transduction efficiency between cells identified by *CellPose* vs. labeled by each of the two human observers (AD and CW; first 2 columns); and between the two human observers (3rd column). A total of 5 slices of 5 different mice were used for each of the 4 model systems. Dashed lines indicate identity. In each case, two measures of agreement are reported: Pearson's correlation coefficient, denoted as r; and the distance between observers, denoted as $d = \sqrt{\sum_i (x_i - y_i)^2}$ where x and y correspond to observers' reports (**a**) or derived quantities (**b**, **c**), and i to the brain slice. Error bars denote the standard error of the mean (with $n = 5$).

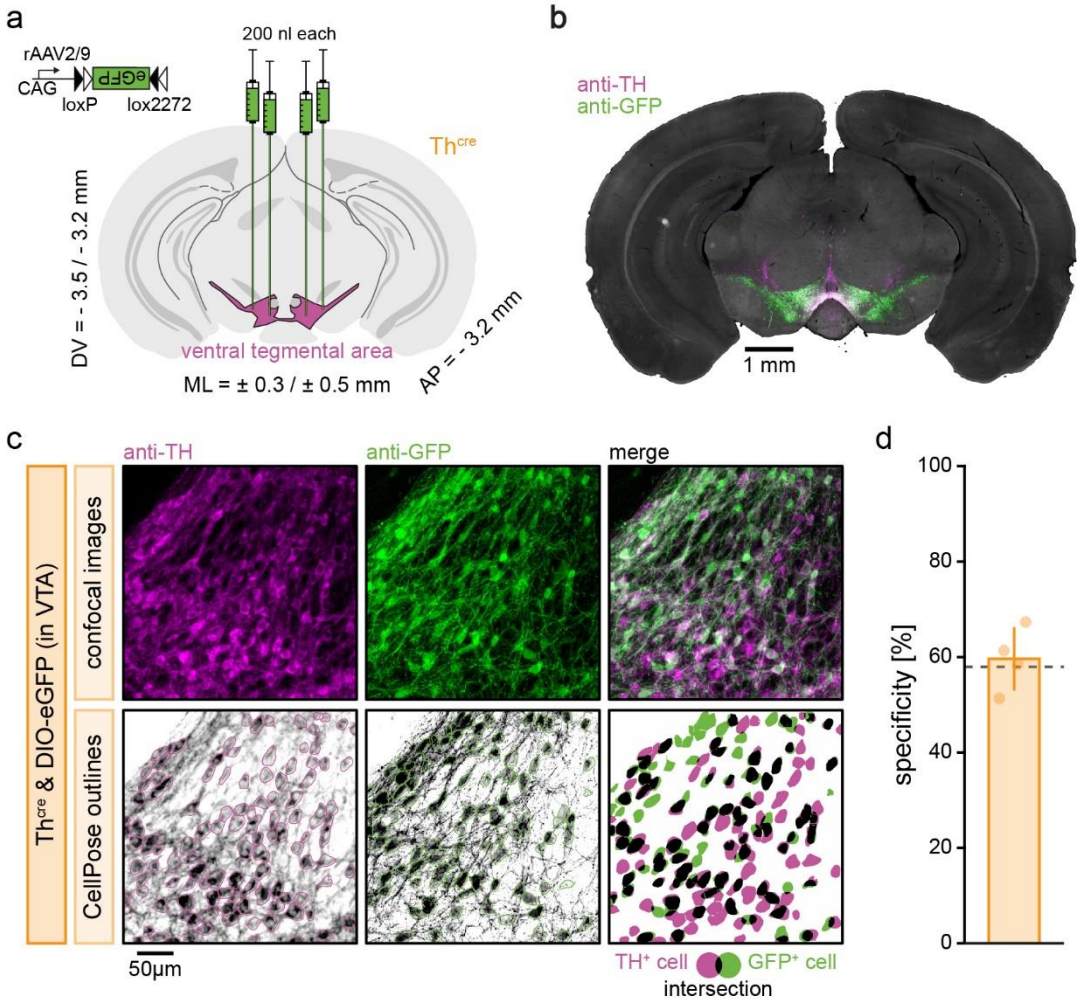

Figure S6 | Specificity of cre-dependent transgene expression in the VTA of *TH^cre^* mice. a, Injection scheme: CAG-DIO-eGFP was bilaterally injected into the VTA of *TH^cre^* mice. **b,** Example of a coronal brain slice stained against TH (magenta) to visualize dopaminergic neurons of the VTA and eGFP (green) to enhance the native fluorescence of eGFP expression. **c,** Exemplary confocal images of VTA-DA neurons in *TH^cre^* mice (top), along with corresponding cell masks as segmented by *CellPose* (bottom). Overlaid cell masks of both channels are shown at the bottom right, where each TH^+ cell was labeled as GFP^+ (successful transduction, black) when cell masks overlapped 50% or more the size of the TH^+ cell, or GFP^- otherwise (missed transduction, magenta). GFP^+ and TH^- (erroneous transduction, green) was counted as unspecific transduction. **d,** The average specificity of GFP expression in the VTA of *TH^cre^* mice amounted to 61.7 ± 6.8 % (derived from a total of 2469 TH^+ and 1627 $eGFP^+$ neurons obtained from 25 images of n = 4 mice). These findings are in line with the specificity of 59 ± 1 % (dashed line) reported by Lammel and colleagues (based on visual inspection)[39]. Numerical data underlying panel d can be found in supplementary material 1 (S1_Data.xlsx).

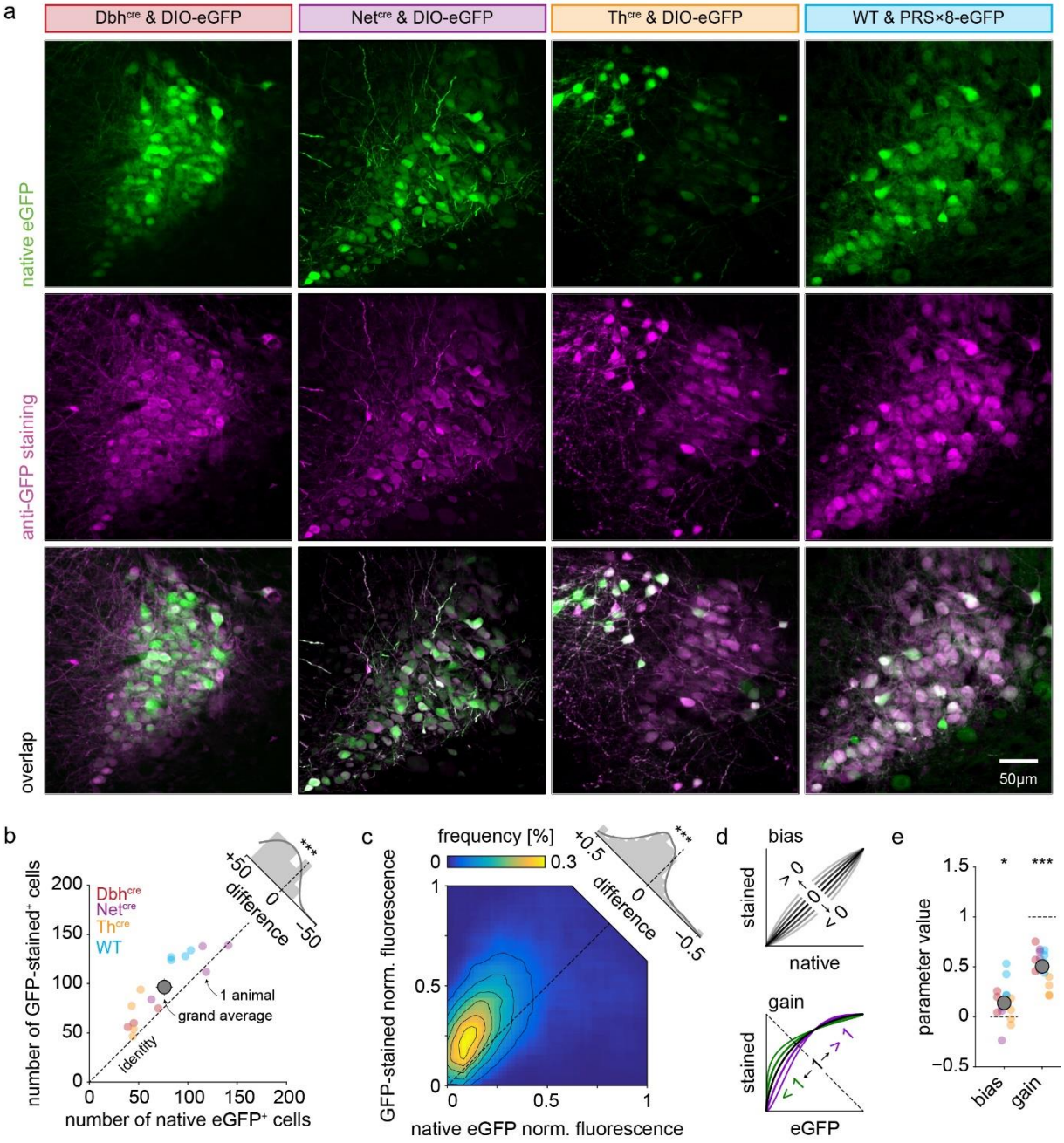

Figure S7 | Comparison of native *eGFP* expression with anti-*GFP* staining. a, Example images of brain slices showing native *eGFP* fluorescence (green, top) and anti-*GFP* immunofluorescence with a secondary antibody in the red spectrum (magenta, center) in *Dbh*^{cre}, *Net*^{cre}, *Th*^{cre} and PRS×8 mice (from left to right). **b**, Number of neurons detected by *CellPose* in the native *eGFP* (green, x-axis) and *GFP*-stained (red, y-axis) channels across animals (n = 3/4/4/4 *Dbh*^{cre}/*Net*^{cre}/*Th*^{cre}/ PRS×8 mice, respectively). 21.5 ± 15.3% more cells were detected in the GFP-stained channel as compared to the native eGFP channel (absolute difference: 20.5 ± 16.5 cells; t-test against 0: $t_{14} = 4.8$, $p = 2.8 \times 10^{-4}$). **c,** Distribution of normalized fluorescence in anti-GFP stained channel as a function of the normalized fluorescence in the native eGFP channel across cells. Fluorescence was averaged within each cell mask (detected in the GFP-stained channel), then binned into 50 × 50 equally spaced bins, and further smoothed by a 2D 10 × 10 boxcar function. The averaged normalized brightness of immune-stained cells per animal (0.40 ± 0.06) exceeded the averaged normalized brightness of the native eGFP-expressing cells (0.26 ± 0.06) by 55 ± 35% (absolute difference: 0.13 ± 0.076; t-test against 0: $t_{14} = 6.66$, $p = 1.08 \times 10^{-5}$). **d**, To quantify the difference in fluorescence between the anti-GFP immunostaining and native eGFP fluorescence in more details, we fitted a non-linear function describing the fluorescence of GFP-stained cells as a function of native eGFP fluorescence (after within-channel normalization, see panel c). The function is of the form $f'_R = \phi(\text{bias} + \text{gain} \times \phi^{-1}(f_G))$, where f_R and f_G denotes the fluorescence in the red (*GFP*-stained) and green (native *eGFP*) channels respectively, and ϕ corresponds to the normal cumulative distribution function.

The ‘bias’ parameter quantifies the overall change in fluorescence induced by the immunostaining (top panel), while the ‘gain’ parameter accounts for a possible asymmetry in the fluorescence increase depending on the native *eGFP* fluorescence (bottom panel). **e**, Estimated parameter values from the function presented in **d**. The ‘bias’ parameter was significantly larger than 0, indicating an increase in fluorescence following *GFP*-staining (0.14 ± 0.19; *t*-test against 0: $t_{14} = 2.85$, $p = 0.013$). The ‘gain’ parameter was significantly smaller than 1, indicating that the increase in fluorescence was substantially stronger for the dimmest cells in the native *eGFP* channel (0.50 ± 0.17; *t*-test against 1: $t_{12} = -11.56$, $p = 1.5 \times 10^{-8}$). In **b**, **c**, and **f**, error bars denote the standard error of the mean (with $n = 15$), while statistical significance is denoted by */**/*** for $p < 0.05/0.01/0.001$, respectively. Numerical data underlying panel e can be found in supplementary material 1 (S1_Data.xlsx).

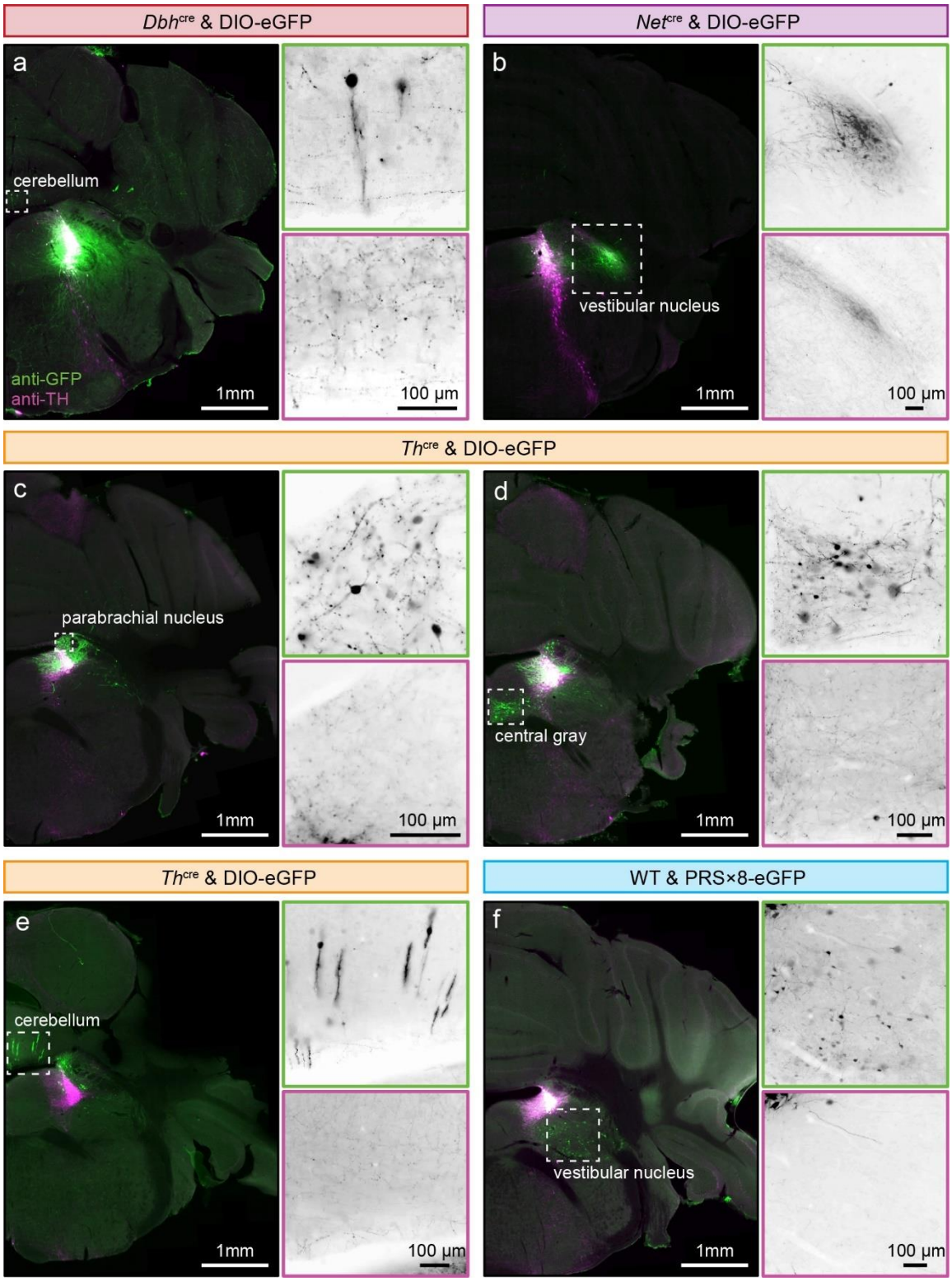

Figure S8 | Ectopic transgene expression across model systems. Example brain slices showing ectopic expression upon *Dbh*^{cre} (**a**), *Net*^{cre} (**b**), *Th*^{cre} (**c-e**), and PRS×8 (**f**) mediated transgene expression. Immuno-straining against TH and GFP is displayed in magenta and green respectively. Insets show inverted gray scale images for a better contrast.

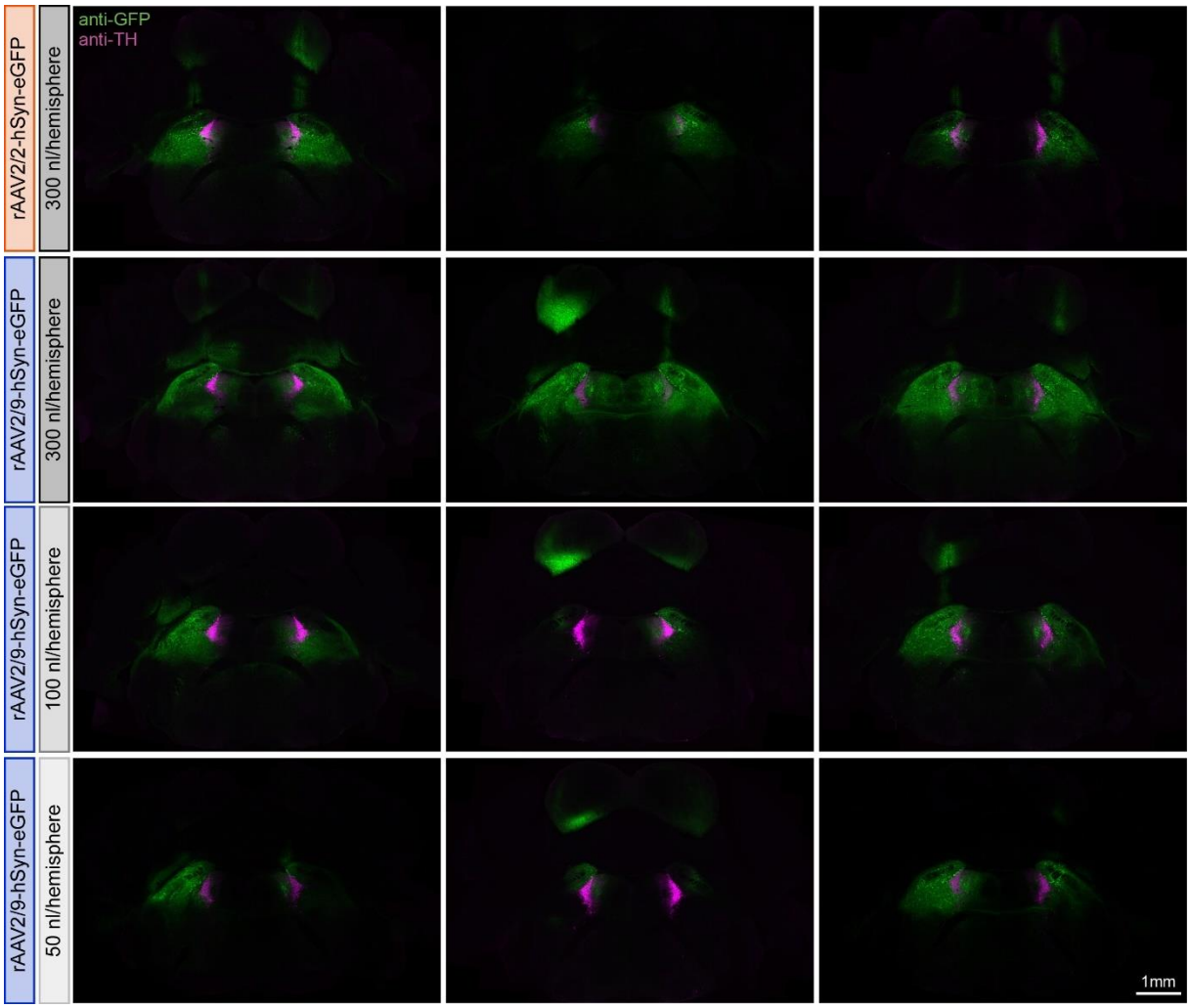

Figure S9 | Effects of serotype and injection volume on viral spread. Coronal brain slices of three wildtype mice that were bilaterally injected with 300 nl of rAAV2/2-hSyn-eGFP (top row), 300 nl of rAAV2/9-hSyn-eGFP (second row from top), 100 nl of rAAV2/9-hSyn-eGFP (third row from top), or 50 nl of rAAV2/9-hSyn-eGFP (bottom row). All slices were stained against tyrosine hydroxylase to visualize LC-NE neurons (magenta) and against eGFP to enhance the native fluorescence of transgene expression (green).

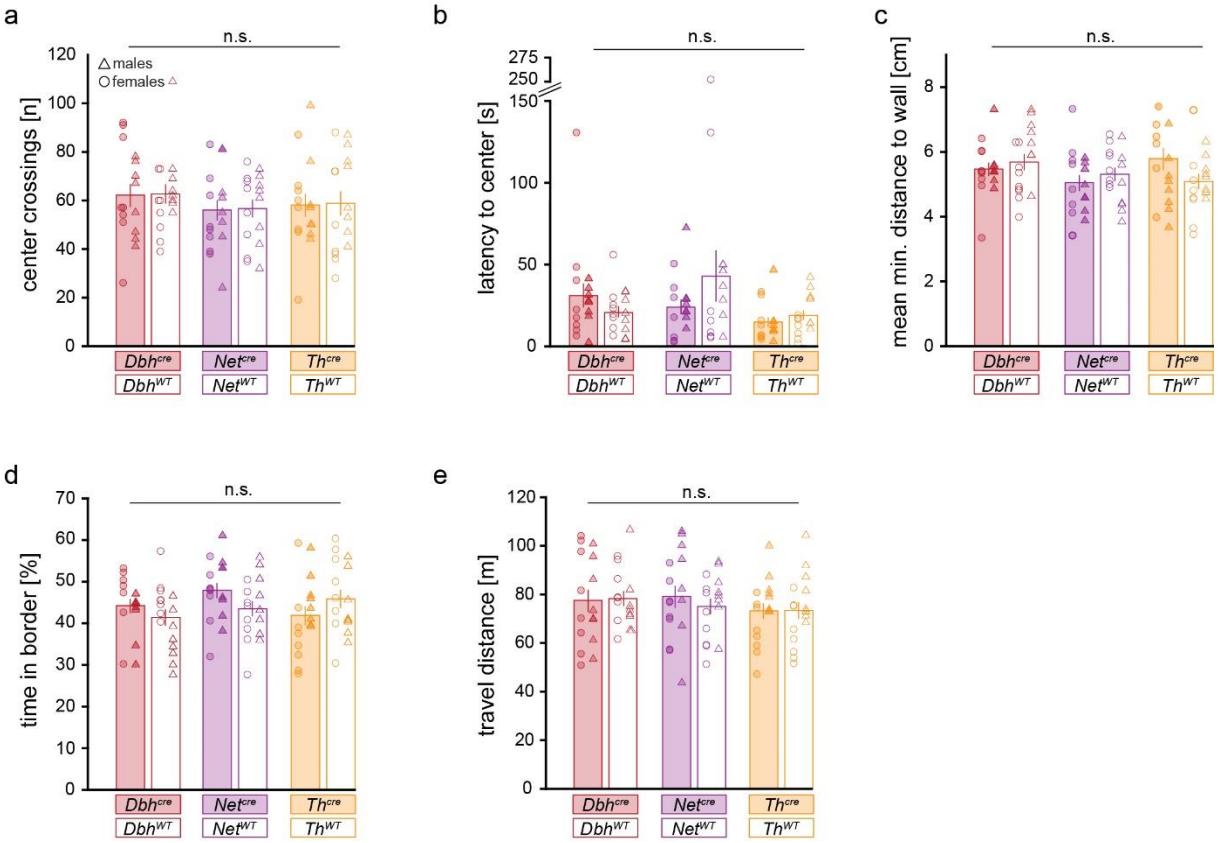

Figure S10 | Supplementary readouts obtained in the open field test. No effect of genotype could be detected on anxiety-like behavior as approximated by **(a)** the number of center crossings, **(b)** the latency to the first center crossing, **(c)** the mean minimum distance to the wall, **(d)** the percentage of time spent in the border of the arena, nor to general locomotion behavior as approximated by **(e)** the total distance travelled by the mouse. All data is depicted as mean ± standard error of the mean. n.s. = not significant. *n* = 8 females (circles) and 8 males (triangles). Numerical data underlying this figure can be found in supplementary material 1 (S1_Data.xlsx).

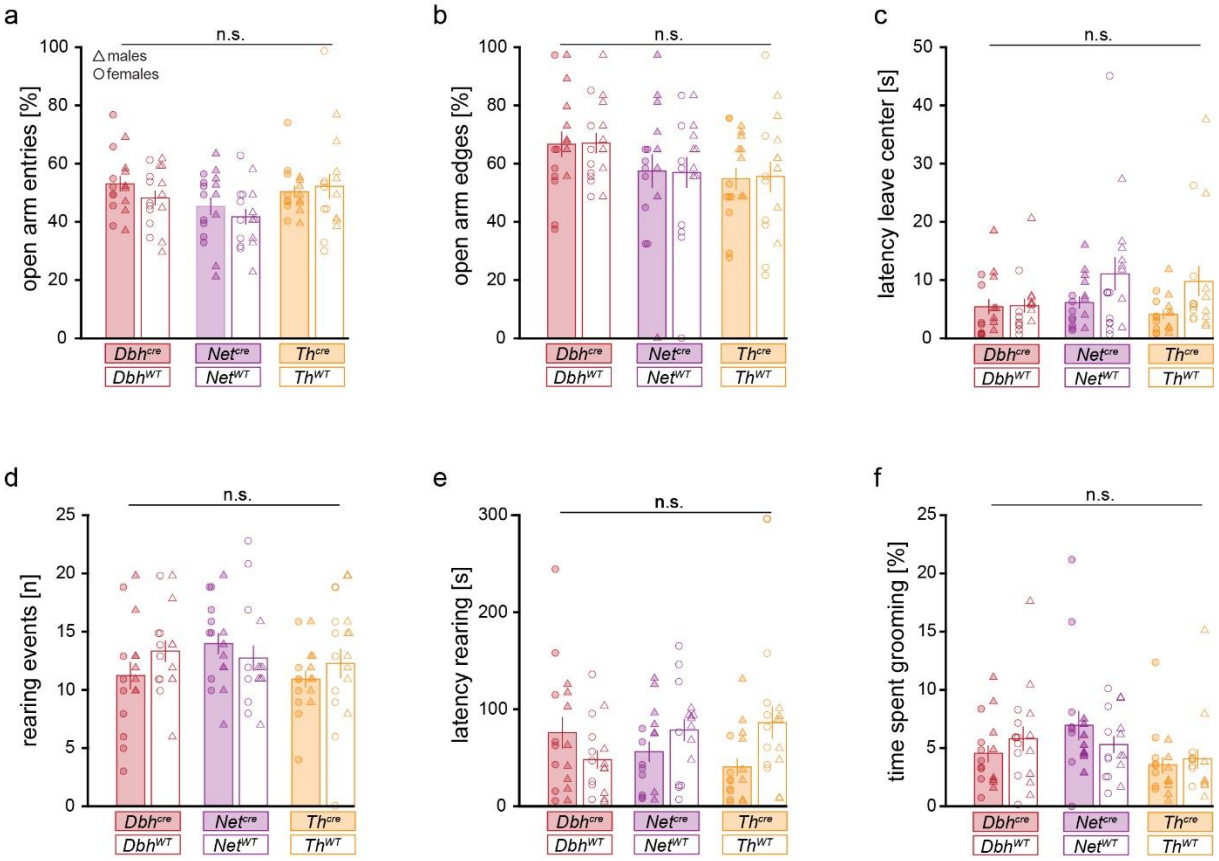

Figure S11 | Supplementary readouts obtained in the elevated plus maze. No effect of genotype could be detected on anxiety-like behavior as approximated by **(a)** the number of open arm entries, **(b)** the percentage of open arm entries on which the animal went to the distant edge of the arm, **(c)** the latency to leave the central platform, **(d)** the number of rearing events, **(e)** the latency to the first rearing event, or **(f)** the percentage of time spent grooming. All data is depicted as mean ± standard error of the mean. n.s. = not significant. *n* = 8 females (circles) and 8 males (triangles). Numerical data underlying this figure can be found in supplementary material 1 (S1_Data.xlsx).

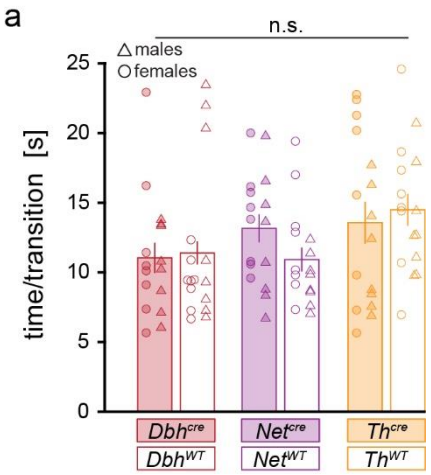

Figure S12 | Supplementary readouts obtained in the Y-maze. No effect of genotype could be detected on locomotion or explorative behavior as approximated by **(a)** the average time per transition between Y-maze arms. All data is depicted as mean ± standard error of the mean. n.s. = not significant. *n* = 8 females (circles) and 8 males (triangles). Numerical data underlying this figure can be found in supplementary material 1 (S1_Data.xlsx).

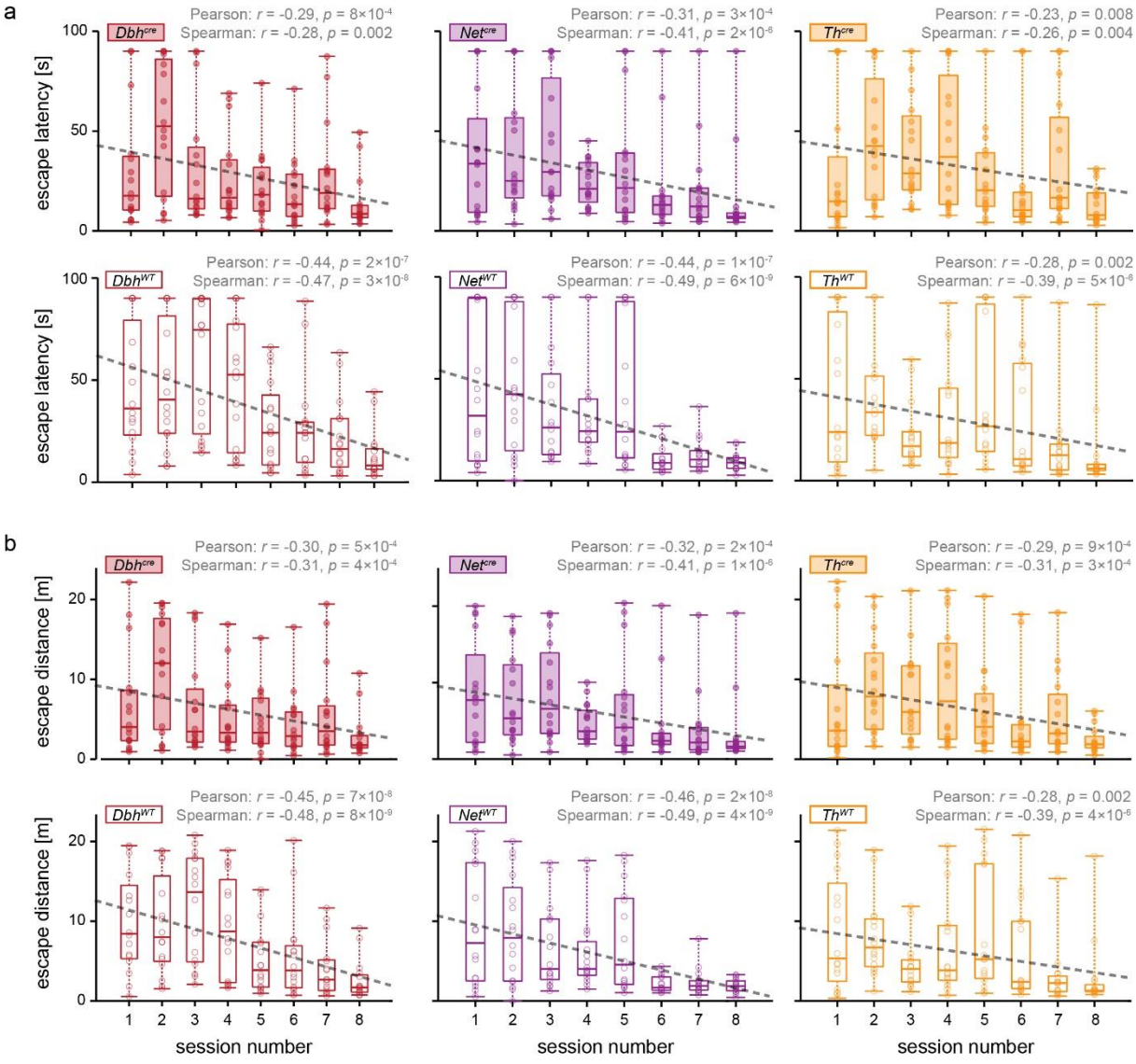

Figure S13 | Morris water maze during training sessions. In each group (n = 16 mice/group), both the latency to reach the platform **(a)** and the distance until the platform was reached **(b)** decreased as a function of training session number (4 sessions were performed on each day for two subsequent days), as indicated by both Pearson's and Spearman's correlation, indicating successful spatial learning in the water maze. Boxplots depict 0/25/50/75/100 percentiles, respectively. Dashed lines indicate the linear fit according to the method of least squares. Numerical data underlying this figure can be found in supplementary material 1 (S1_Data.xlsx).

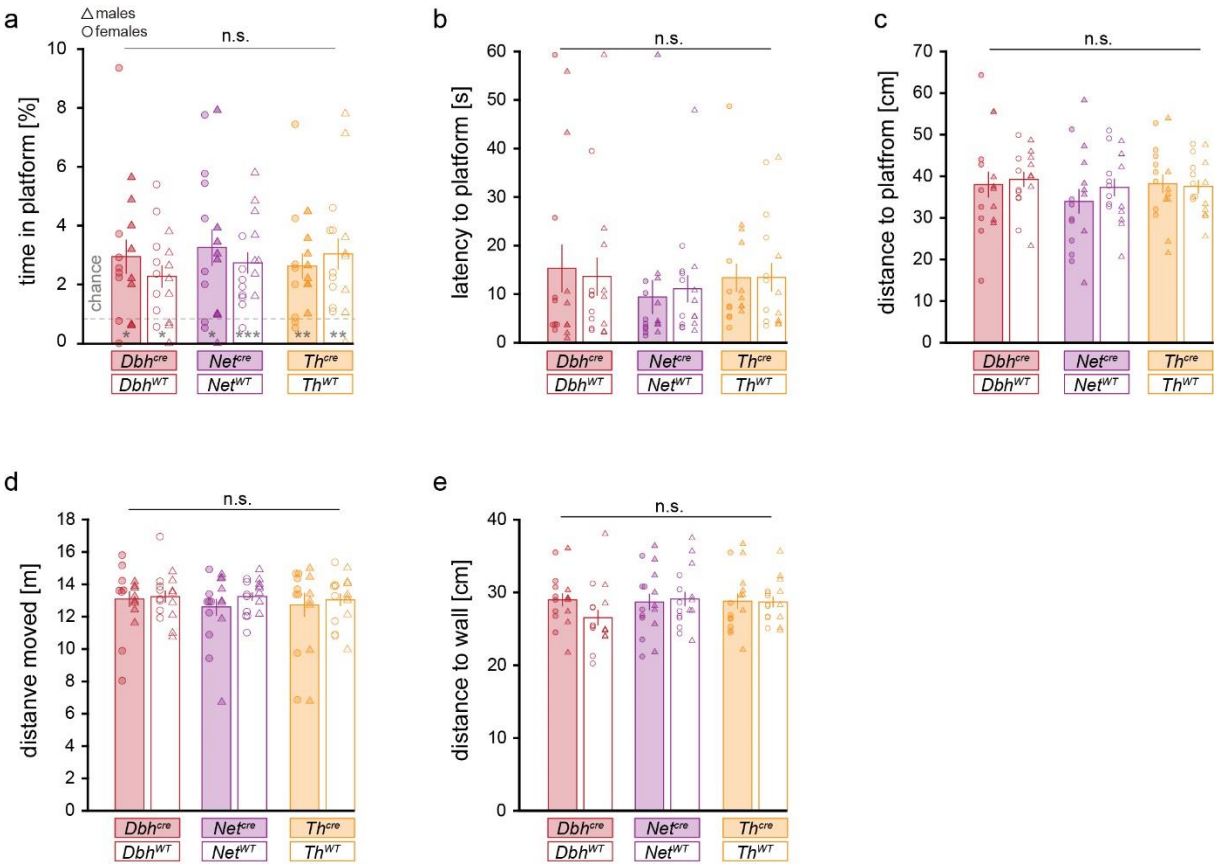

Figure S14 | Supplementary readouts obtained in the Morris water maze. No effect of genotype could be detected on spatial memory as approximated by **(a)** the time spent in the platform area, **(b)** the time needed to reach the platform, and **(c)** the mean minimal distance to the platform. No effect of genotype could be detected on locomotion behavior as approximated by **(d)** the total distance travelled. No effect of genotype could be detected on **(e)** the average distance to the wall, suggesting comparable thigmotactic behavior of mice. All data is depicted as mean ± standard error of the mean. n.s. = not significant. *n* = 8 females (circles) and 8 males (triangles). */**/***, depicted in panel a, for $p < 0.05/0.01/0.001$, respectively, tested against chance level. Numerical data underlying this figure can be found in supplementary material 1 (S1_Data.xlsx).